

Clement Kleinstreuer¹

Department of Mechanical and
Aerospace Engineering,
North Carolina State University,
Raleigh, NC 27695-7910;
Joint Department of Biomedical Engineering,
University of North Carolina at Chapel Hill
and NC State University,
Raleigh, NC 27695-7910
e-mail: ck@ncsu.edu

Yu Feng

Department of Mechanical and
Aerospace Engineering,
North Carolina State University,
Raleigh, NC 27695-7910

Computational Analysis of Non-Spherical Particle Transport and Deposition in Shear Flow With Application to Lung Aerosol Dynamics—A Review

All naturally occurring and most man-made solid particles are nonspherical. Examples include air-pollutants in the nano- to micro-meter range as well as blood constituents, drug particles, and industrial fluid-particle streams. Focusing on the modeling and simulation of inhaled aerosols, theories for both spherical and nonspherical particles are reviewed to analyze the contrasting transport and deposition phenomena of spheres and equivalent spheres versus ellipsoids and fibers. [DOI: 10.1115/1.4023236]

Keywords: lung-aerosol dynamics, nonspherical particles, particle transport and deposition

1 Introduction

The shape and size of inhaled particles, together with a subject's respiratory tract geometry and breathing patterns, greatly determine the particle motion and subsequent airway deposition. This in turn, followed by barrier mass transfer into systemic regions, may have a strong health impact depending on the particles' localized concentrations and whether they are toxic or therapeutic. Although most investigations assumed particles to be perfectly spherical, nonspherical particles, such as fibers, ellipsoids and disks, exhibit quite different airway trajectories and hence deposition patterns in terms of local wall concentrations and propensity for mass transfer and clearance. In particular, ellipsoids and fibers form a unique class of particles, ranging from toxic fibers as in asbestos to carbon nanotubes as well as multifunctional nanoparticles used as drug-carriers. Specifically, respirable fibers are longer than $5\text{ }\mu\text{m}$ and less than $3\text{ }\mu\text{m}$ in diameter with aspect ratios (i.e., fiber length/fiber diameter) larger than three.

Several key factors play simultaneously a role in particle transport and deposition:

(1) Respiratory Tract Geometry.

Geometric variations have a strong impact on the flow field, i.e., different subject-specific airway-geometries will generate unique airflow patterns and hence cause different particle deposition regions, due to impaction as well as secondary flows, diffusion, and/or gravity. Also, certain configurations of the larynx or partial airway occlusion due to diseases may induce high local Reynolds numbers for a given peak inlet velocity, leading to transitional and turbulent flows.

(2) Breathing Pattern.

Inhalation/exhalation waveforms, maximum, and mean air velocities and breathing frequencies may greatly influence the fluid-particle dynamics.

(3) Particulate Characteristics.

As expected, particle size, shape, density, hygroscopicity, and surface properties have a major impact on particle transport and the dominant form of deposition. For example, with inertial impaction being the major mechanism of fiber deposition, the rotation of nonspherical particles is an important transport mechanism, as it can lead to temporal changes in the particle's drag force.

(4) Interaction Phenomena.

Assuming typically dilute particle suspensions, one-way coupling between the fluid flow field and the particle trajectories is assumed. However, in many industrial cases complex fluid-particle, particle-particle, and particle-wall interaction phenomena have to be considered. An example would be three-phase flow of inhaled drug-aerosols depositing in the moving mucus layer.

2 Inhaled Nonspherical Particle Effects

Before launching into various theories describing inhaled particle transport, comparing spherical, effectively spherical and nonspherical modeling approaches, health impacts of fibrous-like particles are discussed.

2.1 Particle Toxicology. Cancers of the respiratory system, especially lung cancer, account for more deaths than any other cancer in both men and women [1]. An estimated 160,340 deaths, making up 28% of all cancer deaths, are expected to occur in the United States in 2012 (see Fig. 1). Furthermore, according to the statistical results shown in Fig. 2 [2], chronic lower respiratory diseases, including chronic obstructive pulmonary diseases (COPDs), were the third leading cause of deaths in the United States. Occupational or environmental exposure to cigarette smoke, asbestos, and other fine-to-ultrafine toxic materials is by far the most important risk factor for respiratory diseases.

Airborne particulate matter has been a health concern for many decades. Although nanotechnology creates possibilities to produce materials with great benefits and improved characteristics on the nano-to-micron scales, occupational exposures to those small particulates may adversely affect human health. In fact, an

¹Corresponding author.

Contributed by the Bioengineering Division of ASME for publication in the JOURNAL OF BIOMECHANICAL ENGINEERING. Manuscript received November 9, 2012; final manuscript received December 3, 2012; accepted manuscript posted December 22, 2012; published online February 7, 2013. Editor: Victor H. Barocas.

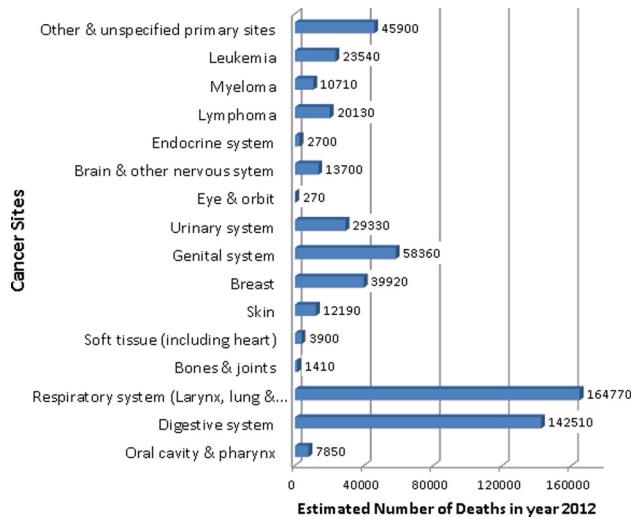


Fig. 1 Estimated number of 2012 deaths caused by different cancers in the United States [1]

association has been demonstrated between inhaled ultrafine particles and various diseases leading to increased morbidity and mortality [3]. For example, nanomaterial structures are more likely to have larger toxic effects than the same materials of conventional sized samples because of their more uniform deposition pattern, deeper migration into the lung, and rapid transport into systemic regions. Specifically, inhaled nanoparticle deposition in lung airways is more uniformly distributed in human lung airways compared to microparticles [4,5]. Due to their small size, nanoparticles can cross biological barriers, such as the air-blood barrier, and therefore can reach cells and tissues normally protected [6]. Furthermore, not only the particle size plays a significant role on its potential health hazards, but so is the particle shape. As indicated, irregular nonspherical particles are found in many industrial particulate flows, such as man-made vitreous fibers (MMVFs) which are being manufactured to replace asbestos [7] as well as carbon nanotubes and drug-aerosols. Fibers are widely used in various industrial fields due to their low cost and highly desirable physical/chemical properties [8]. However, fibers are also associated with potential health hazards when they are inhaled and deposited in the human respiratory system [9]. For example, glass wool fibers in cigarette filters have been found lodged in the soft tissue of the deeper lung, which may develop tumors and cancerous cells.

Most respirable particulate matters deposited in the alveolar region of the lung are cleared by scavenging alveolar macrophages that phagocytize particles and transport them out of the lung, mainly via the muco-ciliary “escalator” lining the airways. Fibers present a special clearance challenge. When inhaled, fibers tend to line up with the air stream in the airways, and hence their effective aerodynamic diameter more closely approximates particle diameter than length. Thus, even relatively long fibers deposit in the alveolar regions if their diameter is small enough. Faced with the challenge of removing long fibers that exceed their physical capacity, macrophages engage in “frustrated” phagocytosis, spilling digestive enzymes and other cellular contents into the alveolar space and initiating pathophysiologic processes that may lead to inflammation, fibrosis and other malignancies. It follows that several major fiber characteristics, that determine fiber toxicity, are dose, dimension, and durability. Highly durable, very long respirable fibers are expected to cause more harm than short and less durable respirable fibers - all else being equal.

Several serious lung diseases are caused by fiber inhalation. For example, malignancies (bronchogenic carcinoma and mesothelioma) and pulmonary fibrosis can be induced by inhalation of asbestos fibers [10]. Several respiratory system related cancers, i.e., lung cancer, laryngeal cancer, pharyngeal cancer, etc., are also considered causally related to asbestos exposure [11]. Concerning multiwall carbon nanotubes (MWCNTs), it has been reported that due to their similar properties to asbestos [12], it is highly possible that they induce alike pulmonary diseases.

In summary, it has now been well documented that fibers, when inhaled, can cause serious diseases [13]. However, consensus was not reached on several topics related to the pathogenicity of fibers; for example, whether *short* fibers ($<5 \mu\text{m}$) play a role in inducing disease. Clearly, the present knowledge base regarding the characteristics that contribute to differences in relative potency between fiber types is incomplete [11]. Consequently, research efforts should be focused on the development of:

- (1) a clearer understanding of the important dimensional and physicochemical determinants of pathogenicity;
- (2) a deeper understanding of the determinants of toxicity for fibers;
- (3) analytical methods that can quantify airborne exposures to fibers.

The study on airborne fibers began with the health hazard evaluation of asbestos used in construction and industry. The use of asbestos fibers was banned by many countries since it was reported in 1970 that the exposure to airborne asbestos fibers increases the incidence of lung cancer, fibrosis, and mesothelioma [7,14–16].

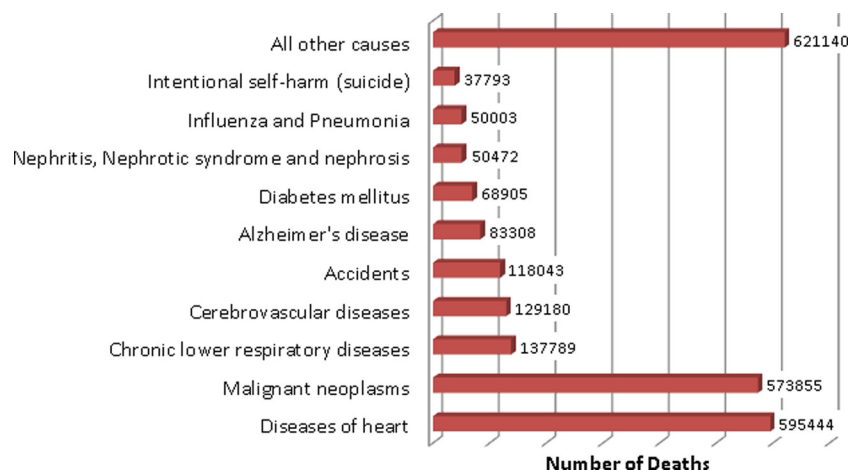


Fig. 2 Deaths for the ten leading causes of deaths in all ages of the United States in 2010 [2]

Man-made vitreous fibers (MMVFs), which are also called man-made mineral fibers and used as alternatives for asbestos, are noncrystalline, fibrous, inorganic substances made primarily from processed minerals [17]. MMVFs such as glass, natural rock, and amorphous silicates, are not nontoxic to humans. The level of the toxicity of MMVFs depends primarily on the fiber dose, fiber dimension, chemical composition, and the bio-persistence in the lungs [14,18]. Based on fiber or ellipsoidal particle transport and deposition characteristics [19], it is reasonable that fiber length (or fiber aspect ratio) has a significant impact on detrimental health effects, mainly because of the ability to penetrate into the deeper lung airways. Additionally, the complex movement of fibers makes it more difficult to predict the pattern of fiber deposition in human airways than the behavior of spherical particles [14].

Carbon nanotubes (CNTs) gained increased attention for their use in material composites, medicine, electronics, and aerospace industries due to superior electrical, mechanical as well as thermal properties. CNTs were first discovered by Sumio Iijima [20]. CNTs can be categorized into two forms: single-wall (SWCNTs) and multiwall carbon nanotubes (MWCNTs) with diameters ranging between 1 to 100 nm and lengths from nanometers to micrometers or even millimeters [21]. They are very light in weight so that they easily suspend in the working environment for a long time, which will raise a potential inhalation exposure hazard [22]. Furthermore, with the decrease in production cost, CNTs will be more and more widely used in daily lives, such as cosmetics, cleaners, electronics, energy-storage devices, solar cells, and filters [9]. On the downside, wastes containing CNTs with low solubility and fibrous characteristics may be released into the environment.

2.2 Therapeutic Impacts of Nonspherical Particles.

Targeted drug delivery and controlled release are current challenges in pulmonary drug delivery. Three popular drug delivery mechanisms are per oral (pill swallowing), intravenous (drug injection into the vein), and inhalation (breathing into the human lung). For pulmonary drug delivery, deposition pattern and clearance are two key aspects for the design of drug formulation and delivery carrier [23]. In particular, the particle shape of drug carriers has a profound impact on optimizing the performance of drug delivery. Compared to spherical particles, fiber-like carriers are more likely to reach the deeper lung airways [24]. Also, fiber-like carriers have shown better internalization abilities than spherical particles for drug delivery [25]. Therefore, it is promising to explore the shape as an important parameter for improved drug delivery performance.

Multifunctional nanoparticles, as well as micron fibers, are also being used as drug carriers for cancer treatment [26]. Existing literature clearly indicates the merits of exploring shape as an important parameter and hints at the exciting prospects of this field [23]. The respiratory system is becoming a more popular drug delivery avenue to combat various diseases such as AIDS, diabetes, and certain cancers. Furthermore, pulmonary drug delivery can be developed as more site-specific and less toxic compared to conventional methods [27–29]. It is also able to effectively combat disorders such as COPD, lung cancer, cystic fibrosis, tuberculosis, and asthma.

Dosimetry, safety, and the efficacy of drugs in the lungs are critical factors in the development of inhaled medicines [30]. Lower deposition fractions are desired in the upper airways for inhaled drugs so that more inhaled medicine particles/fibers can be transported to targeted areas in the deeper lung. To enhance the efficacy of drugs in the lung, the targeting ability and deposition efficiency of different drug carriers (i.e., different size, shapes, and surface properties) in the lung airways are necessary. Specifically, calculations of the airflow in the selected lung geometry using computational fluid dynamics (CFD) and knowing the exact locations of particles/fibers to be deposited in the lung are important information to identify the best drug carriers and inhaler

device that can transport drug aerosols to deeper lung airways and special locations.

For pulmonary drug deliveries, nasal passages are not included and considered because it is rarely used for inhaling pharmaceuticals due to the “highly effective filter” characteristics of the nasal airways [31]. Exceptions are nebulizer for the delivery of drug-aerosol mist into the olfactory region and migration to the brain [32].

2.3 Experimental Evidence. A few experimental and numerical methods have been carried out to investigate fiber transport and deposition in human respiratory systems. For example, Harris and Fraser [33] proposed a model based on the aerodynamic behavior of thin straight rods to estimate lung deposition of fibers. Myojo [34–36] experimentally investigated the deposition of fibers in bronchial airway casts, i.e., single bifurcating tubes based on the third and fourth generation of Weibel’s lung model A [37]. Marijnissen et al. [38] measured nylon fiber transport and deposition in lung airways from the trachea to generation 3 and concluded that particle deposition is roughly similar to that of spherical particles, when focusing on the deposition “hot spots” at the carinas.

The first experimental paper that systematically analyzed the deposition efficiency of asbestos fibers in a human lung-airway replica is that of Sussman et al. [39]. Sussman et al. investigated the effects of fiber diameter and length on the deposition distribution, identifying deposition hot spots such as the posterior wall of the upper trachea and the airway bifurcations.

Su and Cheng [7,15] as well as Zhou et al. [8] experimentally investigated the deposition characteristics of different types of fiber material (i.e., CNTs, TiO_2 , and glass) in two casts of human respiratory systems from mouth to lung airway generation 5. Su and Cheng [7] reported that fibers with lower inertia are more likely to be transported to deeper lung airways, while fibers with higher inertia are more likely to be deposited at the oropharynx wall due to impaction. Moreover, Su and Cheng [7] stated that the fiber deposition efficiency was generally lower than that of spherical particles. In a continuous study of their research group, a good agreement between the experimental results provided by Zhou et al. [8] and Sussman et al. [39] was presented by Zhou et al. [8]. Su and Cheng [15] proposed several empirical deposition efficiency formulas for fibers depositing in different parts of the human respiratory system from mouth to the first generation. All three papers stated that fiber deposition efficiencies increase with higher Stokes numbers, where $\text{St} \sim d_p^2$ [2], v with d_p being the particle effective diameter and v being the mean air-velocity.

3 Theories

Particle motion in a fluid depends on the external force field imposed on the body by the suspending medium or carrier fluid. In direct numerical simulation (DNS), exerted pressure and shear stress distributions on the particle surface are integrated at each time level to obtain the actual force field [40]. If particles deform, as with droplets and free surfaces, or particle build-up is of interest, the volume-of-fluid (VoF) method in conjunction with the PLIC (piecewise-linear interface calculation) scheme may be appropriate. When dealing with dense particle suspensions and the actual particle volume is of importance, the discrete element method (DEM) should be considered for more realistic simulations of inhaled aerosol transport and deposition in subject-specific airway systems [41]. In any case, computationally less taxing is the direct application of Newton’s Second Law of Motion by ignoring the actual particle volume and assuming that point forces act on the body’s mass center. This efficient simulation approach is widely used for spherical particles as well as for nonspherical particles which can be represented by sphere-equivalent particles with modified drag and lift coefficients. Thus, classical particle dynamics for solid spheres with updated correlations for the point forces are reviewed first.

3.1 Spherical Particle Dynamics. For a single particle in shear flow, the particle trajectory equation, i.e., Newton Second Law, can be expressed as [42]:

$$m_p \frac{d\vec{v}_p}{dt} = \sum \vec{F}_{\text{body}} + \sum \vec{F}_{\text{surface}} + \sum \vec{F}_{\text{interaction}} \quad (1)$$

where

$$\frac{d}{dt} = \frac{\partial}{\partial t} + \vec{v}_p \cdot \nabla \quad (2)$$

$$\sum \vec{F}_{\text{body}} = \vec{F}_{\text{Buoyancy}} + \vec{F}_{VM} \quad (3)$$

$$\sum \vec{F}_{\text{surface}} = \vec{F}_D + \vec{F}_{\text{Pressure}} + \vec{F}_{\text{Basset}} + \vec{F}_{\text{Saffman}} + \vec{F}_{\text{Magnus}} \quad (4)$$

$$S\vec{F}_{\text{Interaction}} = \vec{F}_{BM} + \vec{F}_{\text{Particle-particle}} + \vec{F}_{\text{Particle-wall}} \quad (5)$$

Equation (1) is a reduced form of the generalized Basset–Boussinesq–Oseen (BBO) equation discussed by Ref. [43]. The relative importance of each term when compared to the drag force is outlined in Table 1. Still, the BBO equation can be quite complex as it includes a wide range of length scales and time scales, as well as issues concerning turbulence, convection, settling, two-way coupling, collisions, aggregation, etc.

In this section, all expressions are based on the spherical particle assumption. Newton's second law is solved for the particle's trajectory in airflow fields, where multiple polydisperse particles can be individually tracked by solving Eq. (1).

Drag force. To obtain precise motion of a spherical particle, an accurate relationship between Reynolds number and drag force (i.e. drag coefficient) is required. The drag coefficient is introduced as:

$$C_D = \frac{\vec{F}_D}{\frac{\pi d_p^2}{4} \left[\frac{1}{2} \rho_f (\vec{v}_p - \vec{v}_f) |\vec{v}_p - \vec{v}_f| \right]} \quad (6)$$

Thus, the drag force on a spherical particle in “uniform Newtonian fluid flow” can be expressed as [44]:

$$\vec{F}_D = \frac{1}{2} C_D \frac{\pi d_p^2}{4} \rho_f (\vec{v}_p - \vec{v}_f) |\vec{v}_p - \vec{v}_f| \quad (7)$$

with assumptions that the pressure field is uniform and no acceleration is induced by the difference between v_p and v_f . Generally, the *drag coefficient* depends on particle shape and orientation, Reynolds number, and turbulence level, if any. For creeping flow (i.e., $\text{Re}_p < 1$), the Stokes drag force can be written as:

$$\vec{F}_D = 3\pi\mu_f d_p (\vec{v}_p - \vec{v}_f) \quad (8)$$

In nonuniform shear flows and for particles near a wall, drag-force corrections are necessary [44–46], as summarized below. In all cases, the relative particle Reynolds number Re_p is defined as:

$$\text{Re}_p = \frac{|\vec{v}_p - \vec{v}_f| \cdot d_p \cdot \rho_f}{\mu} \quad (9)$$

Specifically, for solid spherical particles,

$$C_D = \begin{cases} \frac{24}{\text{Re}_p}, & 0 < \text{Re}_p < 1 \\ \frac{24}{\text{Re}_p^{0.646}}, & 1 < \text{Re}_p < 400 \end{cases} \quad (10)$$

For spherical droplets,

$$C_D = \frac{3.05(783\kappa^2 + 2142\kappa + 1080)}{(60 + 29\kappa)(4 + 3\kappa)} \text{Re}_p^{-0.74} \quad (11)$$

where $\kappa = \mu_p/\mu_f$. Equation (11) holds for $4 < \text{Re}_p < 100$. Additional correlations were summarized by Loth [47]. For example, White [48] proposed a correlation for C_D in the form of:

Table 1 The relative importance of forces compared to Stokes drag force

Name of the force	Origin of the force	The relative importance compared to Stokes drag force	Negligibility compared to Stokes drag force
\vec{F}_{Basset}	It is a result from the acceleration of the fluid around the particle, i.e., a temporal velocity changes with time. It accounts for the effects of past acceleration on the resistance.	$R_{\text{Basset}} = \left \frac{\vec{F}_{\text{Basset}}}{F_D} \right \sim \sqrt{\frac{\rho_f \tau_s}{\rho_p t}} \tau_s = \frac{\rho_p d_p^2}{18\mu_f}$	$\rho_f \ll \rho_p$ and τ_s is relatively small for submicron particles, it can be neglected
\vec{F}_{Press}	Caused by the pressure gradient	$R_{\text{Pressure}} = \left \frac{\vec{F}_{\text{Pressure}}}{F_D} \right \sim d_p^2 \nabla p$	For submicron particles, since d_p is small and the pressure gradient around the particle can be considered very small, it can be neglected.
\vec{F}_{Faxen}	The near-wall correction term to the Stokes drag force caused by the nonuniform shear field especially near the wall	$R_{\text{Faxen}} = \left \frac{\vec{F}_{\text{Faxen}}}{F_D} \right \sim \left(\frac{d_p}{L} \right)^2$	For submicron particles, since d_p is small, it can be neglected
\vec{F}_{Magnus}	Lift force induced by the particle rotation	$R_{\text{Magnus}} = \left \frac{\vec{F}_{\text{Magnus}}}{F_D} \right \sim \frac{\rho_f d_p^2}{\mu_f} \vec{\omega} $	For submicron particles, since d_p is small, it can be neglected
$\vec{F}_{\text{Buoyancy}}$	Caused by the buoyancy and gravity	$R_{\text{buoyancy}} = \left \frac{\vec{F}_{\text{buoyancy}}}{F_D} \right \sim \frac{(\rho_f - \rho_p) d_p^2}{\mu_f (\vec{v}_f - \vec{v}_p)}$	For submicron particles, it is not neglected; while for nanoparticles, it is neglected.
\vec{F}_{Others}	Including Brownian motion induced force, contact force between particles, etc.	N/A	For submicron particles, Brownian motion force can be neglected; while for nanoparticles, Brownian motion force need to be considered. For dilute particulate suspensions, contact force between particles can be neglected; for dense particulate suspensions, contact force between particles need to be considered.

$$C_D = \frac{24}{\text{Re}_p} + \frac{6}{1 + \sqrt{\text{Re}_p}} + 0.4 \quad \text{Re}_p < 2 \times 10^5 \quad (12)$$

A generally more accurate sub-critical expression (being within 6% of experimental data) was given by Clift and Gauvin [49] as:

$$C_D = \left[\frac{24}{\text{Re}_p} \left(1 + 0.15 \text{Re}_p^{0.687} \right) \right] + \frac{0.42}{1 + \frac{42500}{\text{Re}_p^{1.16}}} \quad \text{Re}_p < 2 \quad (13)$$

Buoyancy. The buoyancy force executed on the particle immersed in the fluid can be expressed as:

$$\vec{F}_{\text{Buoyancy}} = (\rho_f - \rho_p) V_p \cdot \vec{g} \quad (14)$$

Pressure gradient force. The effect of the local pressure distribution gives rise to a force in the direction of the pressure gradient. Therefore, the pressure gradient force \vec{F}_p can be written as [50,51]:

$$\vec{F}_{\text{Pressure}} = \frac{\pi}{6} d_p^3 \nabla p \quad (15)$$

The pressure gradient force is significant only in high-Reynolds number flows.

Virtual mass force. The virtual mass force is a result of the accelerating fluid surrounding the accelerating particle. It has a tendency to keep the particle from being accelerated in any direction. The origin of the force is that the fluid will gain kinetic energy at the expense of the work done by an accelerating submerged particle. It can be expressed as:

$$\vec{F}_{VM} = \frac{1}{2} \rho_f V_p \left(\frac{d\vec{v}_f}{dt} - \frac{d\vec{v}_p}{dt} \right) \quad (16)$$

of which the magnitude is one half of the inertia force for the fluid with the same volume of the particle. It is worth noting that \vec{F}_{vm} can be neglected if the relative acceleration, i.e., $|(d\vec{v}_f/dt) - (d\vec{v}_p/dt)|$ is small. Expressions of the virtual mass force were proposed for cylinders and ellipsoids by Loewenberg [52].

Basset force. The Basset force is due to the lagging boundary layer development with changing relative velocity when particles move through a fluid. It accounts for viscous effects and addresses the temporal delay in boundary layer development as the relative velocity changes with time. It can be rigorously derived from the motion of a single accelerating sphere in the Stokes regime in a quiescent fluid as:

$$\vec{F}_{\text{Basset}} = \frac{3}{2} d_p^2 \sqrt{\pi \rho_f \mu_f} \int_0^t \left(\frac{d\vec{v}_f}{d\tau} - \frac{d\vec{v}_p}{d\tau} \right) \frac{d\tau}{\sqrt{t - \tau}} \quad (17)$$

The Basset force accounts for the effects of past acceleration on the resistance. In the expression, $(-\tau)$ represents the time elapsed since past acceleration from 0 to t [53]. Therefore, this force is due to the diffusion of the vorticity around spherical particles and decays as $t^{-1/2}$, which is typical of diffusion processes. It is also called the history term/force [43].

For $\text{Re}_p > 1$, i.e., beyond the Stokes regime, \vec{F}_{Basset} can be modified by introducing a correction factor. The magnitude ratio between \vec{F}_{Basset} and \vec{F}_D can be written as [53]:

$$R_{\text{Basset}} = \left| \frac{\vec{F}_{\text{Basset}}}{\vec{F}_D} \right| = \sqrt{\frac{18 \rho_f \tau_s}{\pi \rho_p t}} \quad (18)$$

where τ_s is the Stokes relaxation time defined as:

$$\tau_s = \frac{\rho_p d_p^2}{18 \mu_f} \quad (19)$$

\vec{F}_{Basset} can be neglected if $\rho_f \ll \rho_p$ or the Stokes relaxation time is relatively small compared to the time duration from 0 to t .

Lift forces. The total lift coefficient can be defined as [54]:

$$C_L = \frac{F_L}{\frac{1}{8} \rho_f |\vec{v}_f - \vec{v}_p|^2 \pi d_p^2} \quad (20)$$

The total lift force is composed of forces due to different physical mechanisms.

(1) **Saffman Force.**

The Saffman Force is a lift force due to local flow velocity gradients (i.e., shear flows). For small particles translating in a linear unbounded shear field, the expression for the Saffman force's magnitude can be expressed as follows for $\text{Re}_p < 1$:

$$|\vec{F}_{\text{Saffman}}| = \frac{K \mu_f}{4} |\vec{v}_f - \vec{v}_p| d_p^2 \sqrt{\frac{1}{\nu_f} \left| \frac{\partial(\vec{v}_f - \vec{v}_p)}{\partial y} \right|} \cdot \text{sign} \left(\frac{\partial(\vec{v}_f - \vec{v}_p)}{\partial y} \right) \quad (21)$$

$K = 1.615$ is a constant determined based on a numerical integration for creeping flows at low shear rates [55]. The direction of \vec{F}_{Saffman} is either in positive y -direction or negative y -direction. For higher Re_p values or near-wall regions, the expression of the Saffman force needs to be modified.

For creeping flows at low shear rates, the magnitude ratio between \vec{F}_{Magnus} and \vec{F}_D can be written as [53]:

$$R_{\text{Saffman}} = \left| \frac{\vec{F}_{\text{Saffman}}}{\vec{F}_D} \right| = \frac{1.615 d_p}{3\pi} \sqrt{\frac{1}{\nu_f} \left| \frac{\partial(\vec{v}_f - \vec{v}_p)}{\partial y} \right|} \quad (22)$$

It can be neglected when the shear rate is very small or Re_p is very small.

(2) **Magnus Force.**

The Magnus force is a rotation-induced lift force acting on the particle. The expression for such a force is:

$$\vec{F}_{\text{Magnus}} = \frac{1}{8} \pi d_p^2 \rho_f \vec{\omega} \times (\vec{v}_f - \vec{v}_p) \quad (23)$$

where $\vec{\omega}$ is the angular velocity vector of the particle.

The magnitude ratio between \vec{F}_{Magnus} and \vec{F}_D can be written as [53]:

$$R_{\text{Magnus}} = \left| \frac{\vec{F}_{\text{Magnus}}}{\vec{F}_D} \right| = \frac{d_p^2 \rho_f}{24 \mu_f} |\vec{\omega}| \quad (24)$$

Therefore, for small particles (e. g., nanoparticles) the Magnus force can be neglected.

(3) **Wall-Induced Lift Force.**

The hydrodynamic force on a particle moving in a linear shear flow close to a wall is of fundamental significance in fluid dynamics. The effect of the wall is the strongest when the particle is in contact, while the wall effect decays rapidly with distance from the wall [56]. Specifically, the wall-induced lift force is due to two possible mechanisms [46]: (i) the presence of a wall near a particle will break up the axisymmetry of the wake vorticity field, which results in an effective lift force on the particle directed away from the wall; (ii) flow relative to the particle will accelerate faster in the gap between the particle and the wall rather

than further away. The resulting low pressure in the gap (see Bernoulli principle) will induce a lift force directed toward the wall.

Although the wall-induced asymmetry of the flow also induces rotational motion of the particle, many papers claimed that the lift force induced by such a rotation can be neglected when compared to the Saffman force [45,55].

Brownian motion force. $F_{BM,i}$ is the Brownian motion force on the particle in the i -th direction which can be modeled as a Gaussian white noise process [57].

$$F_{BM,i} = \zeta_i \sqrt{\frac{\pi S_0}{\Delta t}} \quad (25)$$

where ζ_i are three zero-mean, unit-variance-independent Gaussian random numbers, Δt is the time step, and S_0 is presented as follows:

$$S_0 = \frac{216 \cdot \nu_f \cdot \kappa_B \cdot T}{\pi^2 \rho_f d_p^5 \left(\frac{\rho_p}{\rho_f}\right)^2 C_c} \quad (26)$$

in which T is the bulk temperature of the mixture, C_c is the Cunningham correction factor:

$$C_c = 1 + \frac{2\lambda}{d_p} \left(1.257 + 0.4 \exp\left(-\frac{1.1d_p}{2\lambda}\right) \right) \quad (27)$$

and κ_B is the Boltzmann constant.

Particle-particle interaction forces. Particle-particle interaction forces are necessary to be considered for dense particle suspensions. Hard sphere model and soft sphere model are the two models which are widely used for numerical simulations [40].

Drag force corrections. For particles in unbounded linear shear flows, the drag force on the particle is not significantly influenced compared to the situation in uniform flows [45]. However, in non-uniform shear field, an additional term for correction, i.e., the Faxen force [44], has to be considered:

$$\vec{F}_{\text{Faxen}} = \mu_f \pi \frac{d_p^3}{8} \nabla^2 \vec{v}_f \quad (28)$$

Zeng [46] indicated that when particles move parallel to a wall, the drag coefficient for all separations between particle and wall can be curve-fitted for all Re_p -numbers as:

$$C_D = \frac{24}{\text{Re}_p} \left(1 + 0.15 \text{Re}_p^{0.687} \right) \left(1 + 0.7005 \exp\left(-2.1 \left(\frac{L}{d_p} - 0.5\right)\right) \right) \quad (29)$$

where L is the distance between the particle and the wall.

Lift force corrections. For Saffman's derivation [55], the lift coefficient can be expressed as:

$$C_L = 5.816 \left(\frac{\alpha^*}{\text{Re}_p} \right)^{\frac{1}{2}} - 0.875 \alpha^* + 2\omega^* \quad (30)$$

Where α^* is the dimensionless shear rate of the fluid:

$$\alpha^* = \frac{d_p}{2|\vec{v}_f - \vec{v}_p|} \frac{\partial v_f}{\partial y} \quad (31)$$

And ω^* is the dimensionless rotational angular speed of the particle

$$\omega^* = \frac{d_p}{2|\vec{v}_f - \vec{v}_p|} \omega \quad (32)$$

As mentioned, Saffman's expression is only suitable for creeping flow. Specifically, experiments [54] suggested that the lift force acts towards the lower-fluid-velocity side from the higher-fluid-velocity side for $\text{Re}_p \gg 1$. The direction of particle movement is exactly opposite to Saffman's expression. McLaughlin [58] extended Saffman's theory to larger Re_p numbers. Dandy and Dwyer [59] numerically studied the drag and lift forces acting on a stationary sphere in a uniform shear flow for $0.1 < \text{Re}_p < 100$. Cherukat et al. [60] investigated spherical particles moving parallel near wall and concluded that the presence of the solid boundary and a large velocity gradient can give rise to a lift force that can affect the trajectory of the aerosol particles.

Based on the theoretical results of Saffman [55] and numerical results obtained by Dandy and Dwyer [59], Mei [61] proposed an expression for the shear lift force on a particle without rotation:

$$\frac{F_L}{F_{\text{saffman}}} = \begin{cases} \left(1 - 0.3314 \alpha^{*\frac{1}{2}} \right) \exp\left(-\frac{\text{Re}_p}{10}\right) + 0.3314 \alpha^{*\frac{1}{2}}, & \text{Re}_p \leq 40 \\ 0.0524 (\alpha^* \text{Re}_p)^{\frac{1}{2}}, & 100 > \text{Re}_p > 40 \end{cases} \quad (33)$$

Kurose and Komori [54] proposed new correlations for the lift coefficient C_L in linear shear flow, considering rotational spherical particles ($1 < \text{Re}_p < 500$):

$$C_L(\text{Re}_p, \alpha^*, \omega^*) = K_0 \alpha^{*0.9} + K_1 \alpha^{*1.1} + (K_2 + K_3 \alpha^* + K_4 \alpha^{*2.0} + K_5 \alpha^{*9.5}) \omega^* \quad (34)$$

where K_0 to K_5 are constants changing with Re_p which can be found in the paper by Kurose and Komori [54] Equation (34) is suitable for $L > 2d_p$. Zeng [45] proposed a C_L -expression for a particle touching the wall ($L = 0.5d_p$) as follow:

$$C_L(\text{Re}_p, \alpha^*, \omega^*) = K_0 \alpha^{*0.9} + K_1 \alpha^{*1.1} + (K_2 + K_3 \alpha^* + K_4 \alpha^{*2.0} + K_5 \alpha^{*9.5}) \omega^* \quad (35)$$

Experimental and numerical studies of the near-wall and non-creeping flow effects on lift forces are ongoing.

3.2 Nonspherical Particle Dynamics Theory. Fibers are particles that have one dimension significantly longer than its other two dimensions [62]. Numerous studies have demonstrated that the fiber aspect ratios as well as fiber durability are critical factors involved in pathogenicity. Therefore, it is important to accurately describe the orientation effect of fibers caused by their rotations. Other than a fiber's translational equation, i.e., Newton's Second law, Eulerian rotational equations must be introduced and solved in order to predict fiber orientation when transported in shear flows.

Complete Numerical Simulation (CNS) Methods. Computational studies of gas-solid flows go back to the very beginning

of CFD [42,44]. However, direct numerical simulation (DNS) methods for multiphase flow have emerged as a major research tool only during the last 20 years [63]. The definition of DNS for multiphase flow is a little confusing. Actually, DNS is a category of simulations which is more often associated with detailed turbulence modeling of the carrier phase with point particle approximations for the dispersed phase [40,63]. Concerning turbulent flow, DNS is a numerical technique to obtain 3D, time-dependent solutions to the nonlinear Navier–Stokes equations [64]. The solution should capture all the scales of turbulence, ranging from large-scale structures to spatial and temporal Kolmogorov-scale turbulence in the flow without employing any empirical closure models.

In this section, detailed numerical simulation of multiphase flows is equivalent to Complete Numerical Simulation (CNS) to avoid confusion with DNS for numerical turbulence analysis [40]. Specifically, CNSs are numerical techniques where the Navier–Stokes equations are applied to finite-size particles instead of introducing “point particle” forces. Joseph [65] indicated that CNS methods for solid-liquid flows are ways of solving the initial value problem for the motion of particles in fluids exactly. Particle movement is described by Newton’s laws under the action of hydrodynamic forces computed from the numerical solution of the fluid flow equations.

Characteristics of CNS methods for multiphase flows can be described as follows. Ideally, all surface and exchange forces should be accurately integrated from the fluid-particle and particle–particle interactions to obtain the velocity, pressure, and stress fields surrounding each particle [42]. Specifically, because scales of meshes for CNS methods are much smaller than the scales of particles, forces such as drag force, lift force, and interaction forces between particles can be obtained directly by *integrating the shear stress and pressure distributed along the particle surfaces without employing any empirical correlations*, such as drag and lift coefficients. Therefore, compared to Euler–Euler models and Euler–Lagrange models, CNS can accurately describe motions of particles with arbitrary shapes on the “meso-scale.” Clearly, CNS of multiphase flows is able to produce detailed results and hence improved knowledge, e. g., the nonlinear and geometrically complicated phenomena of particle–particle and particle–wall interactions [66]. Compared to the Euler–Euler method and Euler–Lagrange method, CNS methods have several advantages:

- (1) The motion of the fluid and that of the solid particles are fully coupled (i.e., two-way coupling). Hence the interactions of both the fluid and the individual solid particles can be calculated.
- (2) Hydrodynamic forces and torques imposed on particles can be obtained by direct integration of the shear stress and pressure distributed along the particle surface without any empirical correlations.

However, the computational cost of the CNS method is still too high for engineering application, especially for a large number of particles in light of the current computational resources available [40]. Thus, in recent years, simplified CNS methods for fluid-solid flows were developed. Several popular approaches, which differ in how to deal with the moving boundaries of the particles (i.e., employing moving meshes), are the arbitrary Lagrangian–Eulerian (ALE) method [66], distributed Lagrange-multiplier (DLM) method [67], and the lattice Boltzmann method (LBM) [68,69].

“Particle Mover” algorithms are essential in realizing CNS methods. Two different kinds of particle movers are widely used: one is based on body-fitted, moving unstructured grids, e.g., the ALE method; another is based on fixed structured grids over which bodies move by a technique involving a system of Lagrange multipliers, e.g., the DLM method. Taking the ALE and DLM methods as examples, details of direct numerical simulations are presented as follows.

(i) *Arbitrary Lagrangian–Eulerian Technique.* The Arbitrary Lagrangian–Eulerian (ALE) technique was first developed by Hu et al. [66]. It can be used to solve particle motions in 2D and 3D flow fields and it can handle particles of different sizes, shapes and materials. In addition, ALE uses a technique based on a combined formulation of the fluid and particle momentum equations, together with a moving, unstructured, finite-element mesh technique to deal with the movement of the particles. The hydrodynamics forces acting on the solid particles are directly computed from the fluid flow field, where the motion of the fluid flow and solid particle trajectories are carefully coupled. The ALE method is also categorized as a boundary-fitted method. Specifically, ALE considers the motion of N rigid solid particles in an incompressible fluid. $\Omega_0(t)$ represents the domain occupied by the fluid at a given time instant t , $t \in [0, T]$, and $\Omega_i(t)$ as the domain occupied by the i th particle ($i = 1, 2, \dots, N$), where $\partial\Omega_0(t)$ and $\partial\Omega_i(t)$ represent the boundaries of $\Omega_0(t)$ and $\Omega_i(t)$ (see Fig. 3).

The governing equations for the fluid motion in $\Omega_0(t)$ can be expressed as follows

Continuity Equation:

$$\nabla \cdot \vec{v}_f = 0 \quad (36)$$

Momentum Equation:

$$\rho_f \frac{D\vec{v}_f}{Dt} = \rho_f \vec{f} + \nabla \cdot \sigma \quad (37)$$

For Newtonian fluids, the stress tensor σ is:

$$\sigma = -p[I] + \mu_f \left[(\nabla \vec{v}_f)^T + \nabla \vec{v}_f \right] \quad (38)$$

where p is the pressure and μ_f is the viscosity of the fluid.

For solid particles of arbitrary shapes, the governing equations differ for each particle i .

Translational Equation:

$$m_{p,i} \frac{d\vec{v}_{p,i}}{dt} = \vec{F}_{\text{body}} + \vec{F}_{\text{surface}} = \vec{F}_{\text{body}} - \int_{\partial\Omega_i(t)} \sigma \cdot \vec{n} dS \quad (39)$$

Eulerian Rotational Equation:

$$\vec{T}_i = - \int_{\partial\Omega_i(t)} (\vec{x}_p - \vec{x}_{cp,i}) \times (\sigma \cdot \vec{n}) dS \quad (40)$$

The index i represents different particles; \vec{n} is the unit normal vector on the surface of the particle pointing into the particle, \vec{T}_i are the hydrodynamic torques acting on the particle i , and $\vec{x}_{cp,i}$ is the centroid of particle i . No-slip boundary conditions are imposed at particle–fluid interfaces, i.e.,

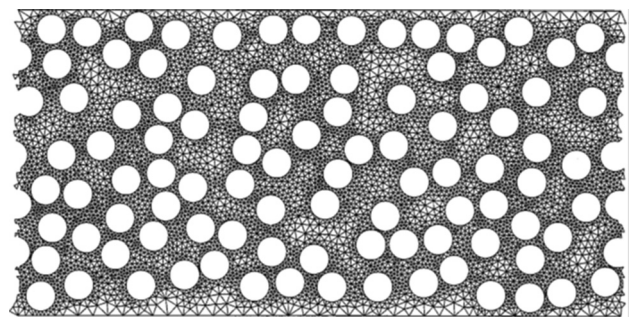


Fig. 3 Two-dimensional finite-element mesh in channel flow using the ALE method [66]

$$\vec{v}_f|_{\partial\Omega_i(t)} = \vec{v}_{p,i} + \vec{\omega}_{p,i} \times (\vec{x}_{p,i} - \vec{x}_{cp,i}) \quad (41)$$

For the fully explicit scheme of the ALE method [70], the solution procedure can be presented as follows:

- Initialization
- Update particle positions
- Re-meshing
- Update flow field, particle velocities, particle angular velocities
- If the time is less than a specified time, repeat from second step on; otherwise, stop

One distinct weakness of the ALE method in its various forms is the need to re-mesh. This prospect alone is a great drain on computational resources and slows the solution process. Therefore, fictitious-domain methods were introduced which can avoid re-generation of the mesh for each time step.

(ii) *Distributed Lagrangian Multiplier Method.* The distributed Lagrange multiplier (DLM) method is based on the fictitious-domain method. The fictitious domain is derived from the idea that fluid fills the space inside of the particles as well as outside. Since fluid fills the whole flow domain, including particle volumes, a simple fixed finite element mesh can be generated to solve for the velocities of the fluid and the particles. As the mesh does not need to be refreshed in every time step, it is much more efficient when compared to the ALE method. The particle is tracked by using boundary control points that are on the particle boundary and move with the particle. The grid (see Fig. 4) does not conform to the shape of the particle. The nodes that are inside the particle boundary have their calculated velocity, i.e., the velocity which at that point in the particle would have due to a rigid body motion. Since fluid occupies the region of the particle, the Navier–Stokes equations must be solved to obtain velocity values for any point inside or on the surface of the particle. The body force term in the Navier–Stokes equations is multiplied by a constant corresponding to that particular position that will yield a velocity due to rigid body motion.

The equations that are solved for the ALE method are also solved for the DLM method. Since the particle is now a fictitious fluid in this method, the motion on the particle boundary and

inside the particle has to match the rigid body motion. To do this, Lagrange multipliers are introduced to multiply the forces on the fluid elements of the particle to make them behave like they are part of a rigid body. These multipliers represent the additional body force needed to maintain rigid-body motion inside the particle boundary. The idea of the distributed Lagrangian multipliers is that the particle is a continuous system and each element must be multiplied by a different constant to properly meet the rigid body motion constraint [65].

Although there is no need for updating meshes at each time step when compared to the ALE method, the computational effort required to solve the equations of motion is higher and therefore somewhat limits the number of particles to be considered.

Euler–Lagrange methods. Euler–Lagrange (E–L) methods, which are also called discrete phase models (DPMs), provide a direct description of the particulate flow by tracking the motion of individual particles [70]. The continuous phase, i.e., fluid flow is governed by continuum equations which can be solved in the Eulerian frame. For spherical particles, their motion is governed by Newton’s Second Law (see Eqs. (1)–(5)) which employs empirical correlations for hydraulic forces acting on the particles. For dilute particle suspensions, one-way coupling is assumed which implies that the particle motion is influenced by the flow field, while the flow field is not disturbed by the presence of the particles [44]. Two types of E–L methods are employed for calculating transport and deposition of a nonspherical particle, i.e., the effective diameter method and the E–L method enhanced with Euler’s rotational equations.

(1) Effective Diameter Method.

Using the “effective diameter method,” nonspherical particles are considered spherical with a parameter-equivalent diameter. Several definitions for “effective diameter” can be found in the literature. They include [19] the equal projected circular area diameter, the equal volume diameter, Stokes equivalent diameter, and aerodynamic diameter. As can be expected, specific empirical correlations for drag force, lift force, and other forces acting on nonspherical particles have to be established.

The effective diameter method can be used as a quick analysis tool for the approximate analysis of nonspherical particle transport and deposition provided that:

- a proper effective/equivalent diameter for nonspherical particles is employed; and
- proper correlations for hydrodynamic forces acting on nonspherical particles are used

Suitable nonspherical hydrodynamic force correlations are summarized as follows:

(i) *Drag Coefficient C_D Correlations for Non-Spherical Particles.* Introducing the shape factor parameter (i.e., sphericity) into the correction of drag coefficient and lift coefficient for nonspherical particle, the shape effect can be captured. Sphericity was first introduced by Wadell [71] and is defined as the ratio of the surface area A_s of a sphere having the same volume V_p as the particle and the actual surface area of the particle A_p :

$$\Psi = \frac{A_s}{A_p} = \frac{\pi^{1/3}(6V_p)^{2/3}}{A_p} = \frac{2\left(\frac{3}{2}\beta\right)^{2/3}}{1+2\beta} \quad (42)$$

For example, for cylindrical particles of height h and radius r , the sphericity is:

$$\Psi_c = \frac{\pi^{1/3}(\pi r^2 h)^{2/3}}{2\pi r(r+h)} = \frac{(rh^2)^{1/3}}{2(r+h)} \quad (43)$$

For ellipsoidal particles with semi-major axis length a and semi-minor axis length b , the sphericity is:

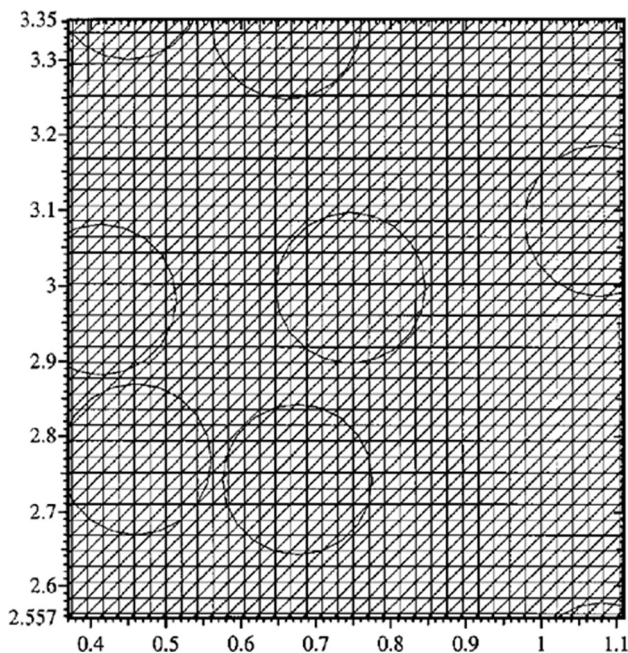


Fig. 4 Fixed triangular grid used in DLM computations [65]

Table 2 Shape factors for non-spherical particles [72]

Shape factor name	Definition	Pros and Cons
Volumetric shape factor (k)	$k = V_p/d_{proj,p}^3$ where $d_{proj,p}$ is the projected area diameter defined as: $d_{proj,p} = \sqrt{4A_{proj,p}/\pi}$ where $A_{proj,p}$ is the projected area of the particle according to its orientation	$A_{proj,p}$ is a difficult parameter to determine because it depends on the orientation of the particle.
Degree of sphericity (Ψ)	$\Psi = A_s/A_p$ where A_s is the surface of a sphere having the same volume as the particle, and A_p is the actual surface area of the particle	A_p is difficult to calculate for particles with irregular shape except for ellipsoidal, cylindrical, and other non-spherical shapes which can be described by mathematical functions.
Degree of circularity (ψ_c)	$\psi_c = P_s/P_{proj,p}$ where P_s is the perimeter of a sphere with equivalent projected area, and $P_{proj,p}$ is the projected perimeter of the particle.	Compared to the degree of sphericity, the circularity can be determined from microscopic or photographic observation.
Aspect ratio (β)	For ellipsoidal particle: $\beta = b_p/a_p$ For cylindrical particle: $\beta = L/d_p$	The aspect ratio can only be used for axisymmetric particles, or else, it is inadequate to describe the shape of the particles.
Shape parameter (Σ)	$\Sigma = A_p/A_{proj,p}$	The shape parameter Σ is only adequate for axisymmetric particles with creeping flow parallel to the axis of symmetry.

$$\Psi_e = \frac{2\sqrt{ab^2}}{a + \frac{b^2}{\sqrt{a^2 - b^2}} \ln\left(\frac{a + \sqrt{a^2 - b^2}}{b}\right)} \quad (44)$$

Other parameters (see Table 2) which can describe the shape factors of nonspherical particles were summarized by Gabitto and Tsouris [72].

Additionally, crosswise sphericity Ψ_{\perp} is defined as the ratio between the cross-sectional area of the volume equivalent sphere and the projected cross-sectional area of the considered particle perpendicular to the flow [73]. Furthermore, lengthwise sphericity Ψ_{\parallel} is defined as the ratio between the cross-sectional area of the volume equivalent sphere and the difference between half the surface area and the mean longitudinal (i.e. parallel to the flow direction) projected cross-sectional area of the considered particle.

Analytical solutions for the drag coefficient of a particle only exist for spheres and spheroids [73] in creeping flow (i.e., $Re_p \ll 1$). For higher particle Reynolds numbers or more complicated flow field, drag coefficients can only be determined by experiments or numerical simulations. In creeping flow, drag coefficients for all bodies decrease inversely proportional to the particle Reynolds number Re_p .

A simple correlation of C_D was proposed by Leith [74] for non-spherical objects in creeping flow as:

$$C_D = \frac{8}{Re_p} \frac{1}{\sqrt{\Psi_{\perp}}} + \frac{16}{Re_p} \frac{1}{\sqrt{\Psi}} \quad (45)$$

Based on experimental curve fitting, Haider and Levenspiel [75] proposed the correlation:

$$C_D = \frac{24}{Re_p} \left(1 + A \cdot Re_p^B\right) + \frac{C}{1 + \frac{D}{Re_p}} \quad (46)$$

where

$$A = \exp(2.3288 - 6.4581 \cdot \Psi + 2.4486 \cdot \Psi^2) \quad (47a)$$

$$B = 0.0964 + 0.5565 \cdot \Psi \quad (47b)$$

$$C = \exp(4.9050 - 13.8944 \cdot \Psi + 18.4222 \cdot \Psi^2 - 10.2599 \cdot \Psi^3) \quad (47c)$$

$$D = \exp(1.4681 + 12.2584\Psi - 20.7322\Psi^2 + 15.8855\Psi^3) \quad (47d)$$

Such a correlation is used by ANSYS FLUENT 14.0 as a default for the nonspherical drag law. However, Gabitto and Tsouris [72] stated that Haider and Levenspiel's correlation showed relatively poor accuracy for particles with $\Psi < 0.67$ and fitted for spheres, isometric solids, and disks with a 5.8% root-mean-square (RMS) deviation.

Ganser [76] proposed an expression for nonspherical particle drag coefficient in the form of:

$$C_D = \frac{24}{Re_p K_1 K_2} \left[1 + 0.1118(Re_p K_1 K_2)^{0.6567}\right] + \frac{0.4305}{1 + 3305/(Re_p K_1 K_2)} \quad (48)$$

where

$$K_1 = \left(d_{p,eff}^{proj} / \left(3d_{p,eff}^{vol}\right) + 2 / (3\Psi^{0.5})\right)^{-1} \quad (48a)$$

$$K_2 = 10^{1.8148(-\log \Psi)^{0.5743}} \quad (48b)$$

$d_{p,eff}^{proj}$ is the equal projected area circle diameter normal to the flow direction:

$$d_{p,eff}^{proj} = \sqrt{4A_{p,n}/\pi} \quad (49)$$

$d_{p,eff}^{vol}$ is the equal-sphere volume diameter. Chhabra et al. [77] compared C_D correlations for nonspherical particles with experimental data ($0.09 < \Psi < 1$ and $1e-4 < Re_p < 5e5$). It was indicated that the correlation proposed by Ganser [76] is more accurate (the mean error is 16%) than Haider and Levenspiel [75] and three other correlations [78–80].

A more realistic drag coefficient correlation for cylindrical particles in an arbitrary direction was proposed by Fan et al. [81]:

$$C_D \cos \alpha = \left(\frac{24}{Re_p}\right) \left(0.006983 + 0.6224 Re_p^{-1.046}\right) \left(\frac{\rho_p}{\rho_f}\right)^{-1.537} \times (Ar^*)^{0.8524} \quad (50)$$

Here α is the angle between the major axis of the cylinder and the direction perpendicular to the flow direction and Ar^* is the modified Archimedes number, which is defined as:

$$Ar^* = \frac{g \cdot d_p^3 \cdot (\rho_p - \rho_f)^2}{\mu_f^2} \quad (51)$$

Fan et al.'s [81] correlation apparently has an accuracy of 9.4% under the conditions of aspect ratio $4 < \beta < 50$, particle density $1125 \text{ kg/m}^3 < \rho_p < 8000 \text{ kg/m}^3$, and $Re_p < 40$.

Tran-Cong et al. [82] introduced a surface-equivalent sphere diameter:

$$d_{p,\text{eff}}^{\text{area}} = \sqrt{4A_p/\pi} \quad (52)$$

where A_p is the particle surface area. They also proposed a particle circularity (or surface sphericity) c :

$$c = \frac{\pi d_{p,\text{eff}}^{\text{area}}}{P_p} \quad (53)$$

where P_p is the projected perimeter of the particle in its direction of motion. The drag coefficient for nonspherical particles is then given for $0.15 < Re_p < 1500$, $0.4 < c < 1.0$, $0.8 < (d_{p,\text{eff}}^{\text{area}}/d_{p,\text{eff}}^{\text{vol}}) < 1.5$ as:

$$C_D = \frac{24}{Re_p} \left(\frac{d_{p,\text{eff}}^{\text{area}}}{d_{p,\text{eff}}^{\text{vol}}} \right) \left[1 + \frac{0.15}{\sqrt{c}} \left(\frac{d_{p,\text{eff}}^{\text{area}}}{d_{p,\text{eff}}^{\text{vol}}} Re_p \right)^{0.687} \right] + \frac{0.42 \left(\frac{d_{p,\text{eff}}^{\text{area}}}{d_{p,\text{eff}}^{\text{vol}}} \right)^2}{\sqrt{c} \left[1 + 4.25 \times 10^4 \left(\frac{d_{p,\text{eff}}^{\text{area}}}{d_{p,\text{eff}}^{\text{vol}}} Re_p \right)^{-1.16} \right]} \quad (54)$$

Loth [47] took into account the orientation effect of spheroid particles by measuring C_D in three axisymmetric axial directions. Due to the linearity of the drag in creeping flow conditions, the drag force can be obtained based on a simple combination of the individual components in three axisymmetric axial directions for a spheroid particle in an arbitrary direction towards the flow. However, for higher Re_p numbers, the linear assumption may not be validated. Loth [47] also provided Stokes correction factors for spheroids of different aspect ratios in different directions.

Based on empirical data for fixed and freely falling particles, Hoelzer and Sommerfeld [73] came up with a C_D expression for nonspherical particles:

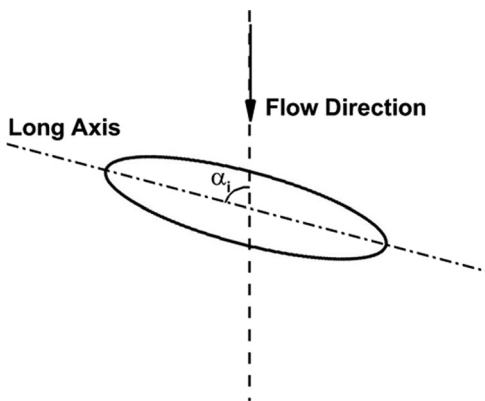


Fig. 5 Incidence angle α_i of nonspherical particle

$$C_D = \frac{8}{Re_p} \frac{1}{\sqrt{\psi}} + \frac{16}{Re_p} \frac{1}{\sqrt{\psi}} + \frac{3}{Re_p} \frac{1}{\sqrt{\psi^{3/4}}} + 0.4210^{0.4(-\log \Psi)^{0.2}} \frac{1}{\Psi_{\perp}} \quad (55)$$

Equation (55) accounts for the particle orientation over the entire range of Reynolds numbers [73].

(ii) *Lift Coefficient Corrections for Non-Spherical Particles.* The theoretical and empirical predictions for the lift coefficient are very limited compared to the information available for drag coefficients. The usual assumption has been to assume that the lift is proportional to the drag and that the dependence with orientation is given by the so-called “cross-flow principle” as suggested by Hoerner [83]:

$$\frac{C_L}{C_D} = \sin^2 \alpha_i \cdot \cos \alpha_i \quad (56)$$

where the incidence angle α_i between the flow direction and the long axis of the fiber-like particle is shown in Fig. 5.

A more “accurate” correlation for the ratio between C_L and C_D was proposed by Mando and Rosendahl [84] as follows:

$$\frac{C_L}{C_D} = \frac{\sin^2 \alpha_i \cdot \cos \alpha_i}{0.65 + 40 Re_p^{0.72}} \quad 30 < Re_p < 1500 \quad (57)$$

However, Mao [85] summarized that the experimental data of the lift force is not sound and hence there is no generally acceptable correlation for the lift coefficient.

Corrections of forces for nonspherical particles can improve the accuracy of numerical simulation results when using the effective diameter method. However, in order to completely capture the orientation effect on the transportation and deposition of nonspherical particles, additional equations, i.e., the Eulerian equations for rotational motion of the rigid body, are necessary. Thus, the Euler–Lagrangian with Euler rotational equation method is now introduced.

(1) Euler–Lagrangian with Euler Rotational Equation Method (EL–ER).

This approach is a good compromise between numerical simulation accuracy and computational cost for simulating nonspherical particle transport and deposition. Based on the Euler–Lagrange method, the Eulerian rotational equations for nonspherical particles are solved with user-enhanced programs [86]. It is worth emphasizing that the EL–ER method employed in the present study is a one-way coupled method which may not be able to accurately predict dense particle suspensions due to the lack of particle–particle interaction representation (see Sec. 4).

The details of this method are shown as follows:

In order to build the computational model for ellipsoidal particle and fiber transport and deposition in different flow fields, the Euler–Lagrange method is employed. Three different Cartesian coordinates are introduced as well as Euler’s quaternions to describe the particle dynamics. The governing equations of the continuous phase as well as the translation equations for ellipsoidal particles are in the global coordinate frame, while rotational equations for ellipsoidal particles are in a body-fixed coordinate frame (see Figs. 6 and 7). Transformation matrices between different coordinates in terms of Euler’s quaternions are introduced as well.

The transformation from a given Cartesian coordinate system to another one can be carried out by means of three successive rotations performed in a specific sequence [87]. The Euler angles (φ , θ , ψ) are then defined as the three successive angles of rotation. The rotation sequence is as follows (see Fig. 6):

- Rotating the initial system of xyz -axes by an angle φ counterclockwise about the z -axis to generate the $\xi\eta\zeta$ -system.

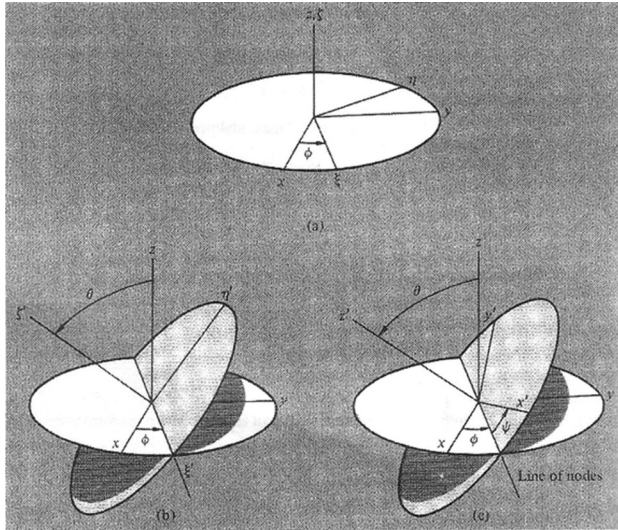


Fig. 6 The rotations defining the Euler angles [87]

- (b) Rotating $\xi\eta\zeta$ about the ξ -axis counterclockwise by an angle θ to produce another intermediate coordinate, i.e., the $\xi'\eta'\zeta'$ -axes.
(c) Rotating $\xi'\eta'\zeta'$ -axes counterclockwise by an angle ψ about the ζ' -axis to produce the desired $x'y'z'$ -system.

Therefore the coordinate transformation between axes $x'y'z'$ and axes xyz can be expressed as:

$$\vec{x'} = A \cdot \vec{x} \quad (58) \quad \text{Simplifying Eq. (59) yields:}$$

$$A = \begin{bmatrix} \cos \psi & \sin \psi & 0 \\ -\sin \psi & \cos \psi & 0 \\ 0 & 0 & 1 \end{bmatrix} \begin{bmatrix} 1 & 0 & 0 \\ 0 & \cos \theta & \sin \theta \\ 0 & -\sin \theta & \cos \theta \end{bmatrix} \times \begin{bmatrix} \cos \phi & \sin \phi & 0 \\ -\sin \phi & \cos \phi & 0 \\ 0 & 0 & 1 \end{bmatrix} \quad (59)$$

$$A = \begin{bmatrix} \cos \psi \cos \phi - \cos \theta \sin \phi \sin \psi & \cos \psi \sin \phi + \cos \theta \cos \phi \sin \psi & \sin \psi \sin \theta \\ -\sin \psi \cos \phi - \cos \theta \sin \phi \cos \psi & -\sin \psi \sin \phi + \cos \theta \cos \phi \cos \psi & \cos \psi \sin \theta \\ \sin \theta \sin \phi & -\sin \theta \cos \phi & \cos \theta \end{bmatrix} \quad (60)$$

The inverse transformation of Eq. (58) can be expressed as:

$$\vec{x} = A^{-1} \cdot \vec{x'} \quad (61)$$

In which A^{-1} is equal to the transpose of matrix A :

$$A^{-1} = \begin{bmatrix} \cos \psi \cos \phi - \cos \theta \sin \phi \sin \psi & -\sin \psi \cos \phi - \cos \theta \sin \phi \cos \psi & \sin \theta \sin \phi \\ \cos \psi \sin \phi + \cos \theta \cos \phi \sin \psi & -\sin \psi \sin \phi + \cos \theta \cos \phi \cos \psi & -\sin \theta \cos \phi \\ \sin \psi \sin \theta & \cos \psi \sin \theta & \cos \theta \end{bmatrix} \quad (62)$$

In order to avoid singularities [19], the transformation matrix A has to be rewritten by introducing Euler's quaternions [87]. The Euler quaternions ($\epsilon_1, \epsilon_2, \epsilon_3, \eta$) are defined as:

$$\epsilon_1 = \cos \frac{\phi - \psi}{2} \sin \frac{\theta}{2} \quad (63a)$$

$$\epsilon_2 = \sin \frac{\phi - \psi}{2} \sin \frac{\theta}{2} \quad (63b)$$

$$\epsilon_3 = \sin \frac{\phi + \psi}{2} \cos \frac{\theta}{2} \quad (63c)$$

$$\eta = \cos \frac{\phi + \psi}{2} \cos \frac{\theta}{2} \quad (63d)$$

where ($\epsilon_1, \epsilon_2, \epsilon_3, \eta$) also satisfies:

$$\epsilon_1^2 + \epsilon_2^2 + \epsilon_3^2 + \eta^2 = 1 \quad (64)$$

Therefore, the transformation matrix A can be rewritten as:

$$A = \begin{bmatrix} 1 - 2(\epsilon_2^2 + \epsilon_3^2) & 2(\epsilon_1\epsilon_2 + \epsilon_3\eta) & 2(\epsilon_1\epsilon_3 - \epsilon_2\eta) \\ 2(\epsilon_2\epsilon_1 - \epsilon_3\eta) & 1 - 2(\epsilon_3^2 + \epsilon_1^2) & 2(\epsilon_2\epsilon_3 + \epsilon_1\eta) \\ 2(\epsilon_3\epsilon_1 + \epsilon_2\eta) & 2(\epsilon_3\epsilon_2 - \epsilon_1\eta) & 1 - 2(\epsilon_1^2 + \epsilon_2^2) \end{bmatrix} \quad (65)$$

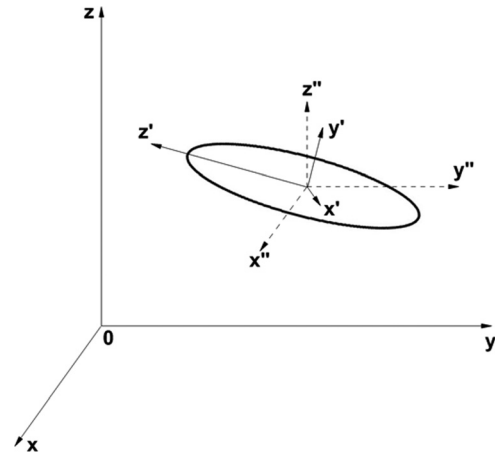


Fig. 7 Coordinate systems for nonspherical particle modeling

in which $\vec{x} = (x, y, z)$, $\vec{x'} = (x', y', z')$ and $A = [a_{ij}]$ is the transformation matrix which can be calculated as:

$(\varepsilon_1, \varepsilon_2, \varepsilon_3, \eta)$ can also be expressed by the elements a_{ij} of the transformation matrix A as follows:

(1) For $\eta \neq 0$:

$$\eta = \pm \frac{1}{2} (1 + a_{11} + a_{22} + a_{33})^{\frac{1}{2}} \quad (66a)$$

$$\varepsilon_1 = \frac{1}{4\eta} (a_{23} - a_{32}) \quad (66b)$$

$$\varepsilon_2 = \frac{1}{4\eta} (a_{31} - a_{13}) \quad (66c)$$

$$\varepsilon_3 = \frac{1}{4\eta} (a_{12} - a_{21}) \quad (66d)$$

(2) For $\eta = 0$:

$$\varepsilon_1 = \pm \sqrt{\frac{1 + a_{11}}{2}} \quad (67a)$$

$$\varepsilon_2 = \frac{a_{12}}{2\varepsilon_1} \quad (67b)$$

$$\varepsilon_3 = \frac{a_{23}}{2\varepsilon_2} \quad (67c)$$

The Euler quaternions will be used instead of Euler angles for modeling nonspherical particle kinematics, indicating the particle orientation in each time step.

As shown in Figs. 7 and 8, three different coordinate systems were introduced for fiber kinematics modeling:

- (1) Space-fixed frame xyz : The inertial coordinate.
- (2) Body-fixed frame $x'y'z'$: The particle coordinate system with its origin being at the particle mass center and its axes being the principal axis.
- (3) Co-moving frame $x''y''z''$: The origin coinciding with that of the body-fixed frame $x'y'z'$ and its axes being parallel to the corresponding axes of the space-fixed frame xyz .

Specifically, there is only relative rotation motion between $x'y'z'$ and $x''y''z''$, while there is only relative translation motion between $x'y'z'$ and xyz . Hence, according to Eq. (58), the transformation between coordinate $x'y'z'$ and $x''y''z''$ can be rewritten as:

$$\vec{x}'' = A \cdot \vec{x}' \quad (68)$$

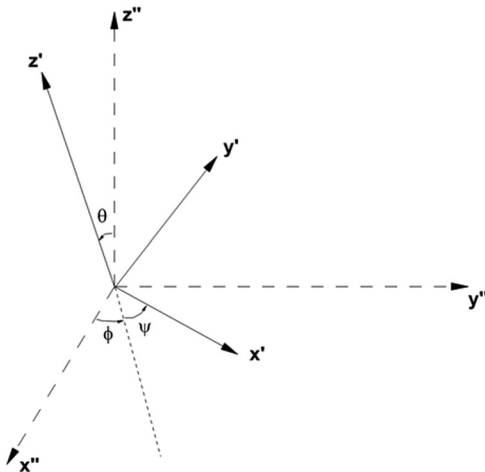


Fig. 8 Euler angles between coordinate $x'y'z'$ and coordinate $x''y''z''$

3.3 Flow Field Governing Equations. The generalized Navier–Stokes equations for the flow field in the global xyz -frame can be expressed as [48]:

$$\nabla \cdot \vec{v}_f = 0 \quad (69)$$

$$\rho_f \frac{D\vec{v}_f}{Dt} = -\nabla p + \mu_f \nabla^2 \vec{v}_f + \rho_f \vec{g} \quad (70)$$

$$\rho_f c_p \frac{DT}{Dt} = k_f \nabla^2 T + \Phi \quad (71)$$

In Eq. (71), Φ is the dissipation function. For Newtonian fluids, Φ can be expressed as:

$$\begin{aligned} \Phi = \mu_f & \left[2 \left(\frac{\partial u_f}{\partial x} \right)^2 + 2 \left(\frac{\partial v_f}{\partial y} \right)^2 + 2 \left(\frac{\partial w_f}{\partial z} \right)^2 + \left(\frac{\partial u_f}{\partial y} + \frac{\partial v_f}{\partial x} \right)^2 \right. \\ & + \left(\frac{\partial w_f}{\partial y} + \frac{\partial v_f}{\partial z} \right)^2 + \left. \left(\frac{\partial u_f}{\partial z} + \frac{\partial w_f}{\partial x} \right)^2 \right] \\ & - \frac{2}{3} \mu_f \left(\frac{\partial u_f}{\partial x} + \frac{\partial v_f}{\partial y} + \frac{\partial w_f}{\partial z} \right)^2 \end{aligned} \quad (72)$$

Clearly, for isothermal fluid flow only Eqs. (69) and (70) are necessary.

3.4 Ellipsoidal Particle Equations. As shown, for spherical particles, only translation equations are needed for tracking each of the spheres. However, due to the anisotropic shapes of nonspherical particles, the orientation has a strong impact on forces executed on the particle [88]. Thus, as discussed, in order to correctly predict forces acting on ellipsoidal and fiber-like particles leading to accurate particle trajectories, Euler rotation equations are necessary for tracking nonspherical particles combined with translation equations. Based on existing papers [19,51,84,89,90], nonspherical particle equations can be formulated as follows.

Translational Equation (in the Global xyz -Frame)

$$m_p \frac{d\vec{v}_p}{dt} = \vec{F}_D + \vec{F}_L + \vec{F}_{BM} + \vec{F}_g + \vec{F}_{\text{other}} \quad (73)$$

where m_p is the mass of the particle, \vec{F}_D is the drag force, \vec{F}_L is the lift force, \vec{F}_{BM} is the Brownian motion induced force, \vec{F}_g is the gravity, and \vec{F}_{other} are other forces which may need to be considered.

Drag force. Specifically, for ellipsoidal particles in Stokes flow, the drag force is:

$$\vec{F}_D = \mu_f \pi a_p [K] \cdot (\vec{v}_f - \vec{v}_p) \quad (74)$$

In Eq. (74), a_p is the semiminor axis of the ellipsoidal particle, \vec{v}_f is the fluid velocity vector at the particle centroid, and $[K]$ is the resistance tensor [91] in the global xyz -frame which can be expressed as:

$$[K] = A^{-1} \cdot [K'] \cdot A \quad (75)$$

Here, $[K']$ is the resistance tensor in the body-fixed frame $x'y'z'$. As axes x' , y' and z' are the principal axes, $[K']$ is a diagonal matrix which can be written as [92]:

$$[K'] = \begin{bmatrix} K'_{11} & 0 & 0 \\ 0 & K'_{22} & 0 \\ 0 & 0 & K'_{33} \end{bmatrix} \quad (76)$$

Table 3 Stokes correction factors for ellipsoidal particles with different aspect ratios

Ellipsoidal particle shape	κ_{ii} value for Major axis parallel to flow direction	κ_{ii} value for Minor axis parallel to flow direction
Oblate exact ($\beta < 1$)	$\frac{(4/3)\beta^{-1/3}(1-\beta^2)}{\left[\frac{(1-2\beta^2) \cdot \cos^{-1} \beta}{\sqrt{1-\beta^2}}\right] + \beta}$	$\frac{(8/3)\beta^{-1/3}(\beta^2-1)}{\beta - \left[\frac{(3-2\beta^2) \cdot \cos^{-1} \beta}{\sqrt{1-\beta^2}}\right]}$
Oblate approximate ($0.25 < \beta < 1$)	$\left(\frac{4}{5} + \frac{\beta}{5}\right)\beta^{-1/3}$	$\left(\frac{3}{5} + \frac{2\beta}{5}\right)\beta^{-1/3}$
Disk ($\beta < 0.25$)	$\frac{8}{3\pi}\beta^{-1/3}$	$\frac{16}{9\pi}\beta^{-1/3}$
Prolate exact ($\beta > 1$)	$\frac{(4/3)\beta^{-1/3}(\beta^2-1)}{\left[\frac{(2\beta^2-1) \cdot \ln(\beta + \sqrt{\beta^2-1})}{\sqrt{\beta^2-1}}\right] - \beta}$	$\frac{(8/3)\beta^{-1/3}(\beta^2-1)}{\left[\frac{(2\beta^2-3) \cdot \ln(\beta + \sqrt{\beta^2-1})}{\sqrt{\beta^2-1}}\right] + \beta}$
Prolate approximate ($6 > \beta > 1$)	$\left(\frac{4}{5} + \frac{\beta}{5}\right)\beta^{-1/3}$	$\left(\frac{3}{5} + \frac{2\beta}{5}\right)\beta^{-1/3}$
Needle Prolate exact ($\beta > 6$)	$\frac{(2/3)\beta^{2/3}}{\ln(2\beta) - 1/2}$	$\frac{(4/3)\beta^{2/3}}{\ln(2\beta) - 1/2}$

with

$$K'_{11} = K'_{22} = \frac{16(\beta^2 - 1)}{\left[(2\beta^2 - 3) \cdot \ln(\beta + \sqrt{\beta^2 - 1}) / \sqrt{\beta^2 - 1}\right] + \beta} \quad (77)$$

and

$$K'_{33} = \frac{8(\beta^2 - 1)}{\left[(2\beta^2 - 1) \cdot \ln(\beta + \sqrt{\beta^2 - 1}) / \sqrt{\beta^2 - 1}\right] - \beta} \quad (78)$$

$\kappa_{ii} = (K'_{ii}/6\beta^{1/3})$ are called “Stokes correction for ellipsoids of aspect ratio β'' [46] or the “dynamic shape factor” which is defined as:

$$\kappa_{ii} = \frac{K'_{ii}}{6\beta^{1/3}} = \frac{F_{D,i}}{3\pi d_{\text{eff},v} \cdot \mu_f (v_{p,i} - v_{f,i})} \quad (79)$$

For ellipsoidal particles with different aspect ratios, expressions of Stokes correction factors are provided in Table 3. K'_{ii} can be replaced using different drag coefficient correlations (e.g., Refs. [73] or [93]). In Eqs. (77) and (78), β is the aspect ratio of the ellipsoidal particle [88]. It is necessary to emphasize that the drag force for nonspherical particle varies its value according to the change of the particle orientation to the flow. Therefore, drag force as well as other forces need to be updated during each time step of the numerical calculation.

Lift Force. The lift force \vec{F}_L acting on an arbitrary-shaped particle is mainly the shear-induced lift force [54]. A general form of Saffman’s lift force for spherical particles can be expressed in tensor form as (see Fig. 9):

$$F_{L,i} = \frac{5.188 \cdot m_p \cdot v_f^{1/2} \cdot D_{ij}}{(\rho_p/\rho_f) \cdot d_p \cdot (D_{kl} \cdot D_{lk})^{1/4}} (v_{f,j} - v_{p,j}) \quad (80)$$

where D_{ij} is the deformation rate tensor which can be expressed as:

$$D_{ij} = \frac{1}{2} \left(\frac{\partial v_{f,i}}{\partial x_j} + \frac{\partial v_{f,j}}{\partial x_i} \right) \quad (81)$$

For modeling nonspherical particle transport and deposition in tubes and channels, especially ellipsoidal particles, only the velocity gradient along the axial direction of the internal flow is considered [19,92]. Several expressions for the lift force \vec{F}_L have been employed:

- (1) Harper and Chang [94]

For the linear shear flow case in which x -direction is the main flow direction and the y -direction is the main shear direction, the lift force can be expressed as:

$$\vec{F}_L = \frac{\pi^2 \mu_f a_p^2}{v_f^{1/2}} \cdot \frac{\partial v_{f,x}/\partial y}{|\partial v_{f,x}/\partial y|^{1/2}} \cdot ([K] \cdot [L] \cdot [K]) \cdot (\vec{v}_p - \vec{v}_f) \quad (82)$$

In Eq. (82), $[K]$ is the resistance tensor in the global xyz -frame is given by Eq. (76), while matrix $[L]$ reads [94]:

$$[L] = \begin{bmatrix} 0.0501 & 0.0329 & 0.00 \\ 0.0182 & 0.0173 & 0.00 \\ 0.00 & 0.00 & 0.0373 \end{bmatrix} \quad (83)$$

For ellipsoidal particles in a general flow field, the lift force (i.e., the Saffman lift force due to the shear stresses) is generated by six velocity gradient components which are $\partial v_{f,x}/\partial y$, $\partial v_{f,x}/\partial z$, $\partial v_{f,y}/\partial x$, $\partial v_{f,y}/\partial z$, $\partial v_{f,z}/\partial x$, and $\partial v_{f,z}/\partial y$. To calculate other lift force components induced by gradients other than $\partial v_{f,x}/\partial y$, Eq. (82) has to be augmented by multiplying the lift force transformation matrix $[B]_{ij}$:

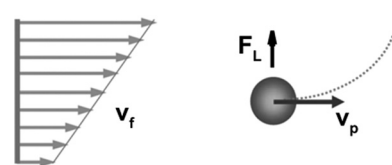


Fig. 9 Saffman lift force for a particle in linear shear flow

Table 4 Lift force transformation matrix $[B]_{ij}$ related to different shear velocity gradients

Shear velocity gradient	Related values of i and j	Related lift force transformation matrix $[B]_{ij}$
$\partial v_{f,x}/\partial y$	$i=1, j=2$	$[B]_{12} = \begin{bmatrix} 1 & 0 & 0 \\ 0 & 1 & 0 \\ 0 & 0 & 1 \end{bmatrix}$
$\partial v_{f,x}/\partial z$	$i=1, j=3$	$[B]_{13} = \begin{bmatrix} 1 & 0 & 0 \\ 0 & 0 & -1 \\ 0 & 1 & 0 \end{bmatrix}$
$\partial v_{f,y}/\partial x$	$i=2, j=1$	$[B]_{21} = \begin{bmatrix} 0 & 1 & 0 \\ 1 & 0 & 0 \\ 0 & 0 & -1 \end{bmatrix}$
$\partial v_{f,y}/\partial z$	$i=2, j=3$	$[B]_{23} = \begin{bmatrix} 0 & 0 & 1 \\ 1 & 0 & 0 \\ 0 & 1 & 0 \end{bmatrix}$
$\partial v_{f,z}/\partial x$	$i=3, j=1$	$[B]_{31} = \begin{bmatrix} 0 & 1 & 0 \\ 0 & 0 & 1 \\ 1 & 0 & 0 \end{bmatrix}$
$\partial v_{f,z}/\partial y$	$i=3, j=2$	$[B]_{32} = \begin{bmatrix} 0 & 0 & -1 \\ 0 & 1 & 0 \\ 1 & 0 & 0 \end{bmatrix}$

$$\vec{F}_L(i, j) = \frac{\pi^2 \mu_f a_p^2}{v_f^{1/2}} \cdot \frac{\partial v_{f,i}/\partial x_j}{|\partial v_{f,i}/\partial x_j|^{1/2}} \cdot \left([K] \cdot [B]_{ij} \cdot [L] \cdot [B]_{ij}^{-1} \cdot [K] \right) \cdot (\vec{v}_p - \vec{v}_f) \quad (i \neq j) \quad (84)$$

Here, i and j denote the three directions of the global coordinates ($i, j = 1, 2, 3$). The lift force transformation matrix $[B]_{ij}$ according to different velocity gradients is shown in Table 4. Thus, the total lift force \vec{F}_L for ellipsoidal particles in a general flow field can be expressed as:

$$\vec{F}_L = \sum_{i,j=1}^3 \vec{F}_L(i, j) \quad (i \neq j) \quad (85)$$

where $\vec{F}_L(i, j)$ can be obtained using Eq. (84). Such a method for calculating the lift force acting on ellipsoidal particles can be employed to solve for the fluid-particle dynamics in human respiratory systems with their complex airflow fields.

(2) Drew et al. [95] and Auton [96]

For a general form of the Saffman force, Drew et al. [95] provided an expression for \vec{F}_L in linear shear flow in the form of:

$$\vec{F}_L = -C_L \cdot V_p \cdot \rho_f \cdot (\vec{v}_p - \vec{v}_f) (\nabla \times \vec{v}_f) \quad (86)$$

For spherical particles, the lift coefficient C_L is equal to 0.50003 [95]. However, for nonspherical particles, the magnitude of C_L has to be measured experimentally or determined numerically.

Brownian motion induced force. As outlined, for spherical particles, $F_{BM,i}$ encapsulates the components of the Brownian-motion induced force in the i -th direction, which can be modeled as a Gaussian white noise process (see Eq. (25)).

For ellipsoidal particles with aspect ratio β , the Brownian motion induced force in three principal directions, i.e., $x'y'z'$ -axes, can be expressed as [57,97]:

$$F_{BM,i'} = \zeta_i \sqrt{\frac{\pi P_{0,i'}}{\Delta t}} \quad (87)$$

where

$$P_{0,x'} = P_{0,y'} = 6\pi\mu_f d_{st,\perp} \cdot \frac{\kappa_B T}{C_c} \quad (88a)$$

$$P_{0,z'} = 6\pi\mu_f d_{st,\parallel} \cdot \frac{\kappa_B T}{C_c} \quad (88b)$$

In which $d_{st,\parallel}$ and $d_{st,\perp}$ denote the Stokes diameters for an ellipsoidal particle oriented parallel and perpendicular to the main drag direction, respectively, and can be expressed as:

$$d_{st,\parallel} = d_{eff,v} \cdot \frac{\frac{4}{3}(\beta^2 - 1)}{\left[\frac{2\beta^2 - 1}{\sqrt{\beta^2 - 1}} \ln\left(\beta + \sqrt{\beta^2 - 1}\right) - \beta \right]} \quad (89a)$$

$$d_{st,\perp} = d_{eff,v} \cdot \frac{\frac{8}{3}(\beta^2 - 1)}{\left[\frac{2\beta^2 - 3}{\sqrt{\beta^2 - 1}} \ln\left(\beta + \sqrt{\beta^2 - 1}\right) + \beta \right]} \quad (89b)$$

Euler Rotation Equations (in body-fixed $x'y'z'$ -frame)

$$I_{x'} \frac{d\omega_{x'}}{dt} - \omega_{y'} \omega_{z'} (I_{y'} - I_{z'}) = T_{x'} \quad (90a)$$

$$I_{y'} \frac{d\omega_{y'}}{dt} - \omega_{z'} \omega_{x'} (I_{z'} - I_{x'}) = T_{y'} \quad (90b)$$

$$I_{z'} \frac{d\omega_{z'}}{dt} - \omega_{x'} \omega_{y'} (I_{x'} - I_{y'}) = T_{z'} \quad (90c)$$

Here, $(I_{x'}, I_{y'}, I_{z'})$ are particle moments of inertia about the principal axes x', y' , and z' ; $(\omega_{x'}, \omega_{y'}, \omega_{z'})$ are particle angular velocities with respect to the principal axes x', y' , and z' ; and $(T_{x'}, T_{y'}, T_{z'})$ are torques acting on the particle with respect to the principal axes x', y' and z' . For ellipsoidal particles, $(I_{x'}, I_{y'}, I_{z'})$ can be written as:

$$I_{x'} = I_{y'} = \frac{(1 + \beta^2) \cdot a_p^2}{5} m_p \quad (91a,b)$$

$$I_{z'} = \frac{2a_p^2}{5} m_p \quad (91c)$$

Hydrodynamics Torque. In simple linear shear flow, $(T_{x'}, T_{y'}, T_{z'})$ are torques acting on the particle with respect to the principal axes x' , y' and z' can be expressed as [98]:

$$T_{x'} = \frac{16\pi\mu_f a_p^3 \beta}{3(\beta_0 + \beta^2 \gamma_0)} \left[(1 - \beta^2) D_{z'y'} + (1 + \beta^2) (W_{z'y'} - \omega_{y'}) \right] \quad (92a)$$

$$T_{y'} = \frac{16\pi\mu_f a_p^3 \beta}{3(\alpha_0 + \beta^2 \gamma_0)} \left[(\beta^2 - 1) D_{x'z'} + (1 + \beta^2) (W_{x'z'} - \omega_{z'}) \right] \quad (92b)$$

$$T_{z'} = \frac{32\pi\mu_f a_p^3 \beta}{3(\alpha_0 + \beta_0)} [W_{y'x'} - \omega_{x'}] \quad (92c)$$

When using Eqs. (92a)–(92c), the underlying assumption is that the flow near the particle on the submicron/nano scale can be approximated as linear shear flow. In Eqs. (92a)–(92c), D_{ij} is the deformation rate tensor, and W_{ij} is the spin tensor. The expressions of D_{ij} and W_{ij} can be given as:

$$[D]_{x'y'z'} = \begin{bmatrix} D_{x'x'} & D_{x'y'} & D_{x'z'} \\ D_{y'x'} & D_{y'y'} & D_{y'z'} \\ D_{z'x'} & D_{z'y'} & D_{z'z'} \end{bmatrix} = \frac{1}{2} \left[\nabla \vec{v}_p + (\nabla \vec{v}_p)^T \right]_{x'y'z'} \quad (93)$$

$$[W]_{x'y'z'} = \begin{bmatrix} W_{x'x'} & W_{x'y'} & W_{x'z'} \\ W_{y'x'} & W_{y'y'} & W_{y'z'} \\ W_{z'x'} & W_{z'y'} & W_{z'z'} \end{bmatrix} = \frac{1}{2} \left[\nabla \vec{v}_p - (\nabla \vec{v}_p)^T \right]_{x'y'z'} \quad (94)$$

Specifically,

$$D_{z'y'} = \frac{1}{2} \left(\frac{\partial v_{p,z'}}{\partial y'} + \frac{\partial v_{p,y'}}{\partial z'} \right) \quad (95a)$$

$$D_{x'z'} = \frac{1}{2} \left(\frac{\partial v_{p,x'}}{\partial z'} + \frac{\partial v_{p,z'}}{\partial x'} \right) \quad (95b)$$

$$W_{z'y'} = \frac{1}{2} \left(\frac{\partial v_{p,z'}}{\partial y'} - \frac{\partial v_{p,y'}}{\partial z'} \right) \quad (95c)$$

$$W_{x'z'} = \frac{1}{2} \left(\frac{\partial v_{p,x'}}{\partial z'} - \frac{\partial v_{p,z'}}{\partial x'} \right) \quad (95d)$$

$$W_{y'x'} = \frac{1}{2} \left(\frac{\partial v_{p,y'}}{\partial x'} - \frac{\partial v_{p,x'}}{\partial y'} \right) \quad (95e)$$

Additionally, in Eqs. (92a)–(92c), α_0 , β_0 , and γ_0 are given as:

$$\alpha_0 = \beta_0 = \frac{\beta^2}{\beta^2 - 1} + \frac{\beta}{2(\beta^2 - 1)^{3/2}} \ln \left[\frac{\beta - \sqrt{\beta^2 - 1}}{\beta + \sqrt{\beta^2 - 1}} \right] \quad (96a)$$

$$\gamma_0 = -\frac{2}{\beta^2 - 1} - \frac{\beta}{(\beta^2 - 1)^{3/2}} \ln \left[\frac{\beta - \sqrt{\beta^2 - 1}}{\beta + \sqrt{\beta^2 - 1}} \right] \quad (96b)$$

Velocity Gradient Transformation. In Eqs. (93) and (94), flow velocity gradients in the body-fixed frame can be obtained by transforming the velocity gradients from the global frame. The velocity gradient transformation $[G]$ from the global frame xyz to the body-fixed frame $x'y'z'$ reads:

$$[G]_{x'y'z'} = A \cdot [G]_{xyz} \cdot A^{-1} \quad (97)$$

where:

$$[G]_{xyz} = \begin{bmatrix} \frac{\partial v_{f,x}}{\partial x} & \frac{\partial v_{f,x}}{\partial y} & \frac{\partial v_{f,x}}{\partial z} \\ \frac{\partial v_{f,y}}{\partial x} & \frac{\partial v_{f,y}}{\partial y} & \frac{\partial v_{f,y}}{\partial z} \\ \frac{\partial v_{f,z}}{\partial x} & \frac{\partial v_{f,z}}{\partial y} & \frac{\partial v_{f,z}}{\partial z} \end{bmatrix} \quad (98a)$$

$$[G]_{x'y'z'} = \begin{bmatrix} \frac{\partial v_{f,x'}}{\partial x'} & \frac{\partial v_{f,x'}}{\partial y'} & \frac{\partial v_{f,x'}}{\partial z'} \\ \frac{\partial v_{f,y'}}{\partial x'} & \frac{\partial v_{f,y'}}{\partial y'} & \frac{\partial v_{f,y'}}{\partial z'} \\ \frac{\partial v_{f,z'}}{\partial x'} & \frac{\partial v_{f,z'}}{\partial y'} & \frac{\partial v_{f,z'}}{\partial z'} \end{bmatrix} \quad (98b)$$

In detail, as $[G]_{xyz}$ satisfies

$$d\vec{v}_p = [G]_{xyz} \cdot d\vec{x} \quad (99)$$

and according to Eq. (61)

$$d\vec{v}_p = A^{-1} \cdot d\vec{v}_p' \quad (100a)$$

and

$$d\vec{x} = A^{-1} \cdot d\vec{x}' \quad (100b)$$

substituting Eqs. (100a) and (100b) to Eq. (99) yields:

$$d\vec{v}_p' = A \cdot [G]_{xyz} \cdot A^{-1} \cdot d\vec{x}' \quad (101)$$

Relationship between Angular Velocities and Euler's Quaternions. The angular velocity components were defined in the body-fixed $x'y'z'$ -frame:

$$\omega_{x'} = \frac{d\psi}{dt} + \frac{d\phi}{dt} \cos \theta \quad (102a)$$

$$\omega_{y'} = \frac{d\theta}{dt} \cos \psi + \frac{d\phi}{dt} \sin \theta \sin \psi \quad (102b)$$

$$\omega_{z'} = \frac{d\phi}{dt} \sin \theta \cos \psi - \frac{d\theta}{dt} \sin \psi \quad (102c)$$

Substituting Eqs. (67a)–(67c) into Eqs. (102a)–(102c) yields:

$$\begin{bmatrix} \frac{d\epsilon_1}{dt} \\ \frac{d\epsilon_2}{dt} \\ \frac{d\epsilon_3}{dt} \\ \frac{d\eta}{dt} \end{bmatrix} = \frac{1}{2} \begin{bmatrix} \eta\omega_{x'} - \epsilon_3\omega_{y'} + \epsilon_2\omega_{z'} \\ \epsilon_3\omega_{x'} + \eta\omega_{y'} - \epsilon_1\omega_{z'} \\ -\epsilon_2\omega_{x'} + \epsilon_1\omega_{y'} + \eta\omega_{z'} \\ -\epsilon_1\omega_{x'} - \epsilon_2\omega_{y'} - \epsilon_3\omega_{z'} \end{bmatrix} \quad (103)$$

Equation (103) is used for updating Euler's quaternions during each time step after the angular velocities have been updated.

3.5 Two-Fluid Euler-Euler Methods. Euler–Euler methods solve two sets of algebraic conservation equations for two different fluids simultaneously for each node in the field [44]. The concept of phasic volume fraction relies on continuous functions of space and time where the sum of volume fractions of each phase is equal to one. Among many Euler–Euler methods, e.g., the Volume-of-Fluid (VOF) model or the Homogeneous Mixture model [42], the two-fluid model is widely used in simulating

fluid-particle flows. Specifically, a set of continuity and momentum equations are solved for each phase with coupling between phases through the pressure and interphase exchange coefficients. The dispersed phase is averaged over each control volume. This approach is used for bubble columns, rises, particle suspensions, and fluidized beds (see, for example, ANSYS FLUENT 14.0, Ansys Inc., Canonsburg, PA). The two-fluid model neglects the discrete nature of the dispersed phase; therefore, it is best suited for high particle volume fractions (larger than 10%), i.e., dense suspensions. Furthermore, there are uncertainties brought by the various closure assumptions; for example, the forms of interaction terms modeling the exchange of mass, momentum and energy between the two phases (i.e., the two “fluids”). Furthermore, appropriate boundary conditions which can characterize the properties of the disperse phase are difficult to determine realistically.

Computational fluid dynamics–discrete element method. As outlined, the Computational Fluid Dynamics–Discrete Element Method (CFD–DEM) which is also called Combined Continuum and Discrete Model (CCDM) [99] is used to compute the stresses and displacements in a volume containing a large number of particles [40,100,101]. The CFD–DEM method was originally proposed for modeling fluidized beds and granular flow. This approach is Lagrangian–Eulerian modeling of the multiphase fluidized medium in which a direct numerical integration of the individual particle trajectories is coupled to a continuum integration of the Navier–Stokes equation of fluid motion via an interphase interaction term [102]. The particle shapes and geometries are specified by the user.

To model particle–particle contact forces, both “hard sphere model” [103,104] and “soft sphere model” (first utilized by Cundall and Strack [100]) were introduced in the CFD–DEM method [40,105,106]. The soft sphere model is very useful for discrete particle simulation of dense phase flows.

In summary, compared with the EL–ER method, CFD–DEM does not provide any advantages in modeling dilute particle suspensions. However, because the CFD–DEM method takes into account particle–particle interaction, it is more accurate than the EL–ER method in simulating more severe conditions, such as large pressure differentials, high velocity gradients as well as intense particle collisions [41,107]. Additionally, the CFD–DEM method can be realized using commercial software such as ANSYS FLUENT 14.0 as a platform by incorporating User Defined Functions (UDF) to the DEM code [99]. Moreover, Fluent, coupled with commercial software EDEM (DEM Solution USA Inc.), can be used for CFD–DEM method realization [41,108].

For multiphase flow predictions in the human respiratory tract, Chen et al. [41] employed CFD–DEM simulations for particle transport and deposition in idealized lung airways and showed good agreement with experimental data. They asserted that CFD–DEM is a suitable method for biological multiphase flow analysis. Additionally, Tao et al. [109] numerically calculated nonspherical granular flow in rectangular hopper using CFD–DEM. Zhou et al. [110,111] employed CFD–DEM for the simulation of fluidization of ellipsoidal particles. Two-way coupled CFD–DEM was discussed by Ren et al. [112].

4 Summary and Comparative Simulation Results

4.1 Summary. In addition to experiments, different numerical methods were introduced to simulate fiber transport and deposition in human respiratory systems. In the past, effective diameter methods were popular, where it is assumed that fibers can be considered as equivalent spherical particles [16] with corrections for the drag force and lift force acting on them. However, the effective diameter method cannot take into account the effect of fiber orientation on the change in drag and lift coefficients during each time step, which is significant for accurate transport and deposition simulation of particulate matter. Tian et al. [113] numerically calculated fiber deposition in an idealized human

lung airway model. They represented fibers as ellipsoidal particles, and their translational and rotational motions were both solved and updated at each time step. The numerical model of Tian et al. [113] considered the orientation effect and provided better predictions than when using the effective diameter method; however, at much higher computational costs. Nevertheless, Tian et al. [113] still used spherical particle deposition mechanisms and their lift force expression was not provided. Specifically, the deposition mechanism in Ref. [113] simplified the ellipsoidal particle as effective spherical particle and did not consider the orientation effect on the deposition judging criteria.

The particle mechanics of ellipsoidal particles is intricate because of the anisotropic shape effect, meaning that the rotational movement must be considered. Ellipsoidal particle transport and deposition in basic shear flows, such as Couette flow and Poiseuille flow, were investigated experimentally and numerically in order to attain more physical insight to the motion characteristics of ellipsoidal particles. For example, Jeffrey [98] investigated ellipsoidal particles in linear shear flow and claimed that the rotation period of the particle is a function of the aspect ratio β and flow shear rate. Gallily and Eisner [114] studied both theoretically and experimentally elongated particles in a 2D Poiseuille flow for the rotation patterns. Chen and Yu [115] proposed a correlation for fiber sedimentation rates in a horizontal circular tube based on their numerical results. Fan and Ahmadi [92] developed models for ellipsoidal particle transport in channels. In continuation, Shanley and Ahmadi [90] studied ellipsoidal particles in steady flow of a horizontal straight pipe, including motion and sedimentation characteristics, and proposed an empirical correlation for particle deposition. Employing the same numerical model from Fan and Ahmadi [92], Tian et al. [19] claimed that ellipsoidal particles transport motion can be affected by the aspect ratio, flow shear rate, as well as particle relative density to the continuous phase, i.e., air. Also, Tian et al. [19] carried out experiments on the deposition efficiency of particles in tubular flow. A similar numerical model was proposed by Yin and Rosendahl [51] but with different expressions for drag force, lift force, and the hydraulic torques. For Yin and Rosendahl’s model, additional assumptions were introduced to express the forces when compared to the model built by Ahmadi’s research group. Höberg et al. [57,116] investigated the Brownian motion effect of submicron ellipsoidal particles. They established a numerical model similar to Fan and Ahmadi [92]; but, made improvements by introducing the Brownian-motion induced force, investigating the fiber transport behavior in steady-state tubular flows. Furthermore, Höberg et al. [117] analyzed micro- and nanofibers transport and deposition in a transient, cyclic tubular flow field, where the transient fluid flow field was based on an analytical solution. They claimed that the fiber-release time during the cyclic flow period has a significant impact on the fiber-deposition efficiency. They also showed that steady-state flow can be used as a good approximation of transient-flow, if an appropriate mean velocity is employed.

4.2 Simulation Results. Using the EL–ER method (see Sec. 3.2) and focusing on spherical versus ellipsoidal particles, Feng [86] numerically investigated the impact of inhaled particle deposition in a subject-specific human airway model (see Fig. 10). The shear stress transport (SST) transition model was employed to solve for the laminar-to-turbulent airflow fields for inlet flow rates ranging from 15 L/min to 60 L/min. ANSYS FLUENT 14.0 with in-house user-defined functions (UDFs) were used to simulate the translational and rotational motion of nonspherical particles/fibers. About 100,000 randomly selected, uniformly distributed fibers were released at the inlet in order to assure that the deposition profiles were independent of the particle count. The total deposition efficiency comparison between spherical and ellipsoidal particles is shown in Fig. 10. The results of the validated computer simulation model clearly indicate that ellipsoidal particles with high aspect ratios (e.g., needle-like fibers) are more dangerous than spherical particles or particles with low aspect

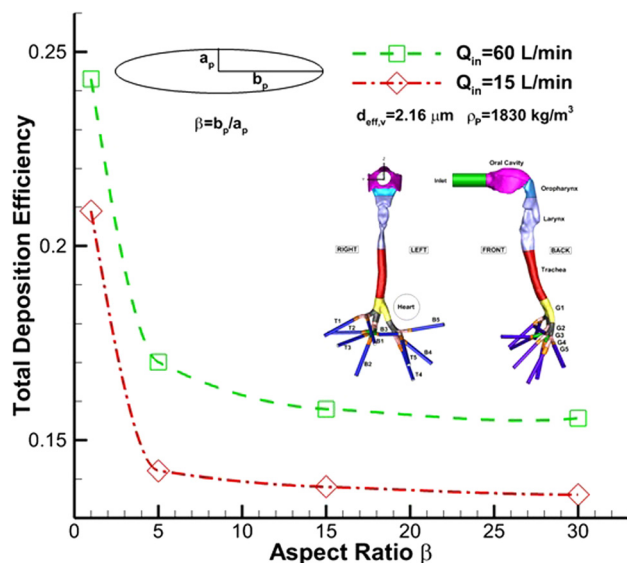


Fig. 10 Total deposition efficiency comparisons between spherical particles and ellipsoidal particles with different aspect ratios in a subject-specific lung airway model [86]

ratios, due to their ability to penetrate into regions of the deeper lung airways. Furthermore, ellipsoidal particle deposition is enhanced as the breathing rate increases.

Acknowledgment

The authors gratefully acknowledge the use of FLUENT software from ANSYS (Canonsburg, PA) and the financial support for Y. F. from NSF, Environmental Health and Safety of Nanotechnology Program, Dr. Barbara Karn, Director.

References

- [1] American Cancer Society, 2012, *Cancer Facts & Figures 2012*, American Cancer Society Inc., Atlanta, GA.
- [2] Murphy, S. L., Xu, J., and Kochanek, K. D., 2012, "Deaths: Preliminary Data for 2010," *Natl. Vital Stat. Rep.*, **60**(4), pp. 1–69. Available at http://www.cdc.gov/nchs/data/nvsr/nvsr60/nvsr60_04.pdf
- [3] Bakand, S., Hayes, A., and Dechsalukthorn, F., 2012, "Nanoparticles: A Review of Particle Toxicology Following Inhalation Exposure," *Inhalation Toxicol.*, **24**(2), pp. 125–135.
- [4] Shi, H., Kleinstreuer, C., Zhang, Z., and Kim, C. S., 2004, "Nanoparticle Transport and Deposition in Bifurcating Tubes With Different Inlet Conditions," *Phys. Fluids*, **16**(7), pp. 2199–2213.
- [5] Zhang, Z., Kleinstreuer, C., Donohue, J. F., and Kim, C. S., 2005, "Comparison of Micro- and Nano-Size Particle Depositions in a Human Upper Airway Model," *J. Aerosol Sci.*, **36**, pp. 211–233.
- [6] Som, C., Wick, P., Krug, H., Nowack, B., 2011, "Environmental and Health Effects of Nanomaterials in Nanotextiles and Façade Coatings," *Environ. Int.*, **37**, pp. 1131–1142.
- [7] Su, W. C., and Cheng, Y. S., 2006, "Deposition of Fiber in a Human Airway Replica," *Aerosol Sci.*, **37**, pp. 1429–1441.
- [8] Zhou, Y., Su, W. C., and Cheng, Y. S., 2008, "Fiber Deposition in the Tracheobronchial Region: Deposition Equations," *Inhalation Toxicol.*, **20**(13), pp. 1191–1198.
- [9] Fenoglio, I., Aldieri, E., Gazzano, E., Cesano, F., Colonna, M., Scarano, D., Mazzucco, G., Attanasio, A., Yakoub, Y., Lison, D., and Fubini, B., 2011, "Thickness of Multiwalled Carbon Nanotubes Affects Their Lung Toxicity," *Chem. Res. Toxicol.*, **25**, pp. 74–82.
- [10] Kamp, D. W., 2009, "Asbestos-Induced Lung Diseases: An Update," *Transl. Res.*, **153**(4), pp. 143–152.
- [11] Gwinn, M. R., Devoney, D., Jarabek, A. M., Sonawane, B., Wheller, J., Weissman, D. N., Masten, S., and Thompson, C., 2011, "Meeting Report: Mode(s) of Action of Asbestos and Related Mineral Fibers," *Environ. Health Perspect.*, **119**(12), pp. 1806–1810.
- [12] Pacurari, M., Qian, Y., Porter, D. W., Wolfarth, M., Wan, Y., Luo, D., and Guo, N. L., 2011, "Multi-Walled Carbon Nanotube-Induced Gene Expression in the Mouse Lung: Association With Lung Pathology," *Toxicol. Appl. Pharmacol.*, **255**(1), pp. 18–31.
- [13] Levy, B. S., Wagner, G. R., and Rest, K. M., eds, 2005, *Preventing Occupational Disease and Injury*, APHA, Washington, DC.

- [14] Wang, Z., Hopke, P. K., Baron, P. A., Ahmadi, G., Cheng, Y. S., Deye, G., and Su, W. C., 2005, "Fiber Classification of the Influence of Average Air Humidity," *Aerosol Sci. Technol.*, **39**, pp. 1056–1063.
- [15] Su, W. C., and Cheng, Y. S., 2009, "Deposition of Man-Made Fibers in Human Respiratory Airway Casts," *Aerosol Sci.*, **40**, pp. 270–284.
- [16] Inthavong, K., Wen, J., Tian, Z., and Tu, J., 2008, "Numerical Study of Fibre Deposition in a Human Nasal Cavity," *Aerosol Sci.*, **39**, pp. 253–265.
- [17] Baan, R. A., and Grosse, Y., 2004, "Man-Made Mineral (Vitreous) Fibres: Evaluations of Cancer Hazards by the IARC Monographs Programme," *Mutat. Res.*, **553**, pp. 43–58.
- [18] Lippman, M., 1990, "Effects of Fiber Characteristics on Lung Deposition, Retention, and Disease," *Environ. Health Perspect.*, **88**, pp. 311–317.
- [19] Tian, L., Ahmadi, G., Wang, Z., and Hopke, P. K., 2012, "Transport and Deposition of Ellipsoidal Fibers in Low Reynolds Number Flows," *J. Aerosol Sci.*, **45**, pp. 1–18.
- [20] Iijima, S., 1991, "Helical Microtubules of Graphitic Carbon," *Nature*, **354**(6348), pp. 56–58.
- [21] Poland, C. A., Duffin, R., Kinloch, I., Maynard, A., Wallace, W. A., Seaton, A., and Donaldson, K., 2008, "Carbon Nanotubes Introduced into the Abdominal Cavity of Mice Show Asbestos-Like Pathogenicity in a Pilot Study," *Nature Nanotechnol.*, **3**(7), pp. 423–428.
- [22] Lam, C. W., James, J. T., McCluskey, R., Arepalli, S., and Hunter, R. L., 2006, "A Review of Carbon Nanotube Toxicity and Assessment of Potential Occupational and Environmental Health Risks," *Crit. Rev. Toxicol.*, **36**, pp. 189–217.
- [23] Mitravotri, S., 2009, Editorial: In drug Delivery, Shape Does Matter," *Pharm. Res.*, **26**(1), pp. 232–234.
- [24] Sturm, R., and Hofmann, W., 2009, "A Theoretical Approach to the Deposition and Clearance of Fibers With Variable Size in the Human Respiratory Tract," *J. Hazard. Mater.*, **170**, pp. 210–218.
- [25] Gratton, S. E., Ropp, P. A., Pohlhaus, P. D., Luft, J. S., Madden, V. J., Napier, M. E., and Desimone, J. M., 2008, "The Effect of Particle Design on Cellular Internalization Pathways," *Proc. Natl. Acad. Sci. USA.*, **105**, pp. 11613–11618.
- [26] Kleinstreuer, C., 2013, *Microfluidics and Nanofluidics: Theory and Selected Applications*, John Wiley & Sons, Hoboken, NJ.
- [27] Kleinstreuer, C., Zhang, Z., and Donohue, J. F., 2008, "Targeted Drug-Aerosol Delivery in the Human Respiratory System," *Ann. Rev. Biomed. Eng.*, **10**, pp. 195–220.
- [28] Kleinstreuer, C., and Zhang, Z., 2010, "Airflow and Particle Transport in the Human Respiratory System," *Ann. Rev. Fluid Mech.*, **42**, pp. 301–334.
- [29] Singh, A., Rishabha, M., and Pramod, K. S., 2011, "Pulmonary Drug Delivery System: A Novel Approach for Drug Delivery," *Current Drug Ther.*, **6**(2), pp. 137–151.
- [30] Forbes, B., Asgharian, B., Dailey, L. A., Ferguson, D., Gerde, P., Gumbleton, M., Gustavsson, L., Hardy, C., Hassall, D., Jones, R., Lock, R., Maas, J., McGovern, T., Pitcaim, G. R., Somers, G., and Wolff, R. J., 2011, "Challenges in Inhaled Product Development and Opportunities for Open Innovation," *Adv. Drug Delivery Rev.*, **63**, pp. 69–87.
- [31] Pollard, A., Uddin, M., Shinnab, A. M., and Ball, C. G., 2012, "Recent Advanced and Key Challenges in Investigations of the Flow Inside Human Oro-Pharyngeal-Laryngeal Airway," *Int. J. Comput. Fluid Dyn.*, **12**, pp. 1–19.
- [32] Shi, H. W., 2006, "Numerical Simulation of Airflow, Particle Deposition and Drug Delivery in a Representative Human Nasal Airway Model," Ph.D. thesis, North Carolina State University, Raleigh, NC.
- [33] Harris, R. L., and Fraser, D. A., 1976, "A model for deposition of fibers in the human respiratory system," *Am. Ind. Hyg. Assoc. J.*, **37**, pp. 73–89.
- [34] Myojo, T., 1987, "Deposition of Fibrous Aerosol in Model Bifurcating Tubes," *J. Aerosol Sci.*, **18**, pp. 337–347.
- [35] Myojo, T., 1990, "The Effect of Length and Diameter on Deposition of Fibrous Aerosol in a Model Lung Bifurcation," *J. Aerosol Sci.*, **21**(5), pp. 651–659.
- [36] Myojo, T., and Takaya, M., 2001, "Estimation of Fibrous Aerosol Deposition in Upper Bronchi Based on Experimental Data With Model Bifurcation," *Indust. Health*, **39**, pp. 141–149.
- [37] Weibel, E. R., 1963, "Principles and Methods for the Morphometric Study of the Lung and Other Organs," *Lab. Invest.*, **12**, pp. 131–155.
- [38] Marijnissen, J., Zeckendorf, A., Lemkowicz, S., and Bibo, H., 1991, "Transport and Deposition of Uniform Respirable Fibres in a Physical Lung Model," *J. Aerosol Sci.*, **22**(1), pp. S859–S862.
- [39] Sussman, R. G., Cohen, B. S., and Lippmann, M., 1991, "Asbestos Fiber Deposition in a Human Tracheobronchial Cast: I. Experimental," *Inhalation Toxicol.*, **3**, pp. 145–160.
- [40] Crowe, C. T., Schwarzkopf, J. D., Sommerfeld, M., and Tsuji, Y., 2011, *Multi-phase Flows With Droplets and Particles*, 2nd ed, CRC Press, Boca Raton, FL.
- [41] Chen, X., Zhong, W., Zhou, X., Jin, B., and Sun, B., 2012, "CFD-DEM Simulation of Particle Transport and Deposition in Pulmonary Airway," *Powder Technol.*, **228**, pp. 309–318.
- [42] Kleinstreuer, C., 2003, *Two-Phase Flow: Theory and Applications*, Taylor and Francis, New York.
- [43] Michaelides, E., 2003, "Hydrodynamic Force and Heat/Mass Transfer From Particles, Bubbles, and Drops—The Freeman Scholar Lecture," *J. Fluids Eng.*, **125**, pp. 209–238.
- [44] Kleinstreuer, C., 2006, *Biofluid Dynamics: Principles and Selected Applications*, CRC Press, Boca Raton, FL.
- [45] Bagchi, P., and Balachandar, S., 2002, "Shear versus Vortex-Induced Lift Force on a Rigid Sphere at Moderate Re," *J. Fluids Mech.*, **473**, pp. 379–388.

- [46] Zeng, L. Y., 2007, "Interaction Between a Spherical Particle and Wall-Bounded Flows at Finite Reynolds Number," Ph.D. thesis, University of Illinois at Urbana-Champaign, Urbana, IL.
- [47] Loth, E., 2008, "Drag of Nano-Spherical Solid Particles of Regular and Irregular Shape," *Powder Technol.*, **182**, pp. 342–353.
- [48] White, F. M., 1991, *Viscous Fluid Flow*, 2nd ed., McGraw-Hill, New York.
- [49] Clift, R., and Gauvin, W. H., 1971, Motion of Entrained Particles in Gas Streams, *Can. J. Chem. Eng.*, **49**(4), pp. 439–448.
- [50] Shimazaki, Y., Okubo, M., Yamamoto, T., and Yoshida, A., 2009, "Three-Dimensional Numerical Simulation of Nanoparticle Inhalation and Indoor Pollution Around Breathing Human," *J. Environ. Eng.*, **4**(1), pp. 145–161.
- [51] Yin, C., Rosendahl, L., Kaer, S. K., and Sorensen, H., 2003, "Modelling the Motion of Cylindrical Particle in a Nonuniform Flow," *Chem. Eng. Sci.*, **58**, pp. 3489–3498.
- [52] Loewenberg, M., 1993, "Stokes Resistance, Added Mass, and Basset Force for Arbitrarily Oriented, Finite-Length Cylinders," *Phys. Fluids*, **5**(3), pp. 765–767.
- [53] Johnson, R. W., 1998, *The Handbook of Fluid Dynamics*, 1st ed., Springer-Verlag GmbH & Co., Heidelberg, Germany.
- [54] Kurose, R., and Komori, S., 1999, "Drag and Lift Forces on a Rotating Sphere in a Linear Shear Flow," *J. Fluid Mech.*, **384**, pp. 183–206.
- [55] Saffman, P. G., 1965, "The Life on a Small Sphere in a Slow Shear Flow," *J. Fluid Mech.*, **22**, pp. 385–400.
- [56] Lee, H., and Balachandrar, S., 2010, "Drag and Lift Forces on a Spherical Particle Moving on a Wall in a Shear Flow at Finite Re," *J. Fluid Mech.*, **657**, pp. 89–125.
- [57] Högberg, S. M., Akerstedt, H. O., Lundstroem, T. S., and Freund, J. B., 2008, "Numerical Model for Fiber Transport in the Respiratory Airways," Proceedings of the 19th International Symposium on Transport Phenomena, Reykjavik, Iceland.
- [58] McLaughlin, J. B., 1991, "Inertial Migration of a Small Sphere in Linear Shear Flows," *J. Fluid Mech.*, **224**, pp. 261–274.
- [59] Dandy, D. S., and Dwyer, H. A., 1990, "A Sphere in Shear Flow at Finite Reynolds Number: Effect of Shear on Particle Lift, Drag, and Heat Transfer," *J. Fluid Mech.*, **216**, pp. 381–410.
- [60] Cherukat, P., McLaughlin, J. B., and Graham, A. L., 1994, "The Inertial Lift on a Rigid Sphere Translating in a Linear Shear Flow Field," *Int. J. Multiphase Flow*, **20**(2), pp. 339–353.
- [61] Mei, R., 1992, "An Approximate Expression for the Shear Lift Force on a Spherical Particle at Finite Reynolds Number," *Int. J. Multiphase Flow*, **18**(1), pp. 145–147.
- [62] Donaldson, K., Aitken, R., Tran, L., Stone, V., Duffin, R., Forrest, G., and Alexander, A., 2006, "Carbon Nanotubes: A Review of their Properties in Relation to Pulmonary Toxicology and Workplace Safety," *Toxicol. Sci.*, **92**(1), pp. 5–22.
- [63] Bunner, B., and Tryggvason, G., 2003, "Effect of Bubble Deformation on the Properties of Bubbly Flows," *J. Fluid Mech.*, **495**, pp. 77–118.
- [64] Crowe, C. T., Troutt, T. R., and Chung, J. N., 1996, "Numerical Models for Two-Phase Turbulent Flows," *Ann. Rev. Fluid Mech.*, **28**, pp. 11–43.
- [65] Joseph, D., 2001, "Interrogations of Direct Numerical Simulation of Solid-Liquid Flow," Technical Report No. 26, University of Minnesota Supercomputing Institute, Minneapolis, MN.
- [66] Hu, H. H., Joseph, D. D., and Crochet, M., 1992, "Direct Simulation of Fluid Particle Motions," *J. Theor. Comput. Fluid Dyn.*, **3**, pp. 285–306.
- [67] Glowinski, R., Pan, T. W., Hesla, T. I., and Joseph, D. D., 1999, "A Distributed Lagrange Multiplier/Fictitious Domain Method for Particulate Flows," *Int. J. Multiphase Flow*, **25**, pp. 755–794.
- [68] Lin, J., Shi, X., and You, Z., 2003, "Effects of the Aspect Ratio on the Sedimentation of a Fiber in Newtonian Fluids," *J. Aerosol Sci.*, **34**, pp. 909–921.
- [69] Li, Z., and Kleinstreuer, C., 2011, "Airflow Analysis in the Alveolar Region Using the Lattice-Boltzmann Method," *Med. Biol. Eng. Comput.*, **49**(4), pp. 441–451.
- [70] Hu, H. H., Patankar, A., and Zhu, M. Y., 2001, "Direct Numerical Simulations of Fluid-Solid Systems Using the Arbitrary Lagrangian-Eulerian Technique," *J. Comput. Phys.*, **169**, pp. 427–462.
- [71] Wadell, H., 1934, The Coefficient of Resistance as a Function of Reynolds Number for Solids of Various Shapes, J. Franklin Institute, **217**, pp. 459–490.
- [72] Gabitto, J., and Tsouris, C., 2008, "Drag Coefficient and Settling Velocity for Particles of Cylindrical Shape," *Powder Technol.*, **183**, pp. 314–322.
- [73] Hölzer, A., and Sommerfeld, M., 2008, "New Simple Correlation Formula for the Drag Coefficient of Non-Spherical Particles," *Powder Technol.*, **184**(3), pp. 361–365.
- [74] Leith, D., 1987, "Drag on Nonspherical Objects," *Aerosol Sci. Technol.*, **6**(2), pp. 153–161.
- [75] Haider, A., and Levenspiel, O., 1989, "Drag Coefficient and Terminal Velocity of Spherical and Nonspherical Particles," *Powder Technol.*, **58**, pp. 63–70.
- [76] Ganser, G. H., 1993, "A Rational Approach to Drag Prediction of Spherical and Nonspherical Particles," *Powder Technol.*, **77**, pp. 143–152.
- [77] Chhabra, R. P., Agarwal, L., and Sinha, N. K., 1999, "Drag on Non-Spherical Particles: An Evaluation of Available Methods," *Powder Technol.*, **101**, pp. 288–295.
- [78] Chien, S. F., 1994, "Settling Velocity of Irregularly Shaped Particles," *SPE Drill. Complet.*, **9**, pp. 281–289.
- [79] Hartman, M., Trnka, O., and Svoboda, K., 1979, "Free Settling of Nonspherical Particles," *Ind. Eng. Chem. Res.*, **33**, pp. 1979–1983.
- [80] Thompson, T. L., and Clark, N. N., 1991, "A Holistic Approach to Particle Drag Prediction," *Powder Technol.*, **6**, pp. 57–66.
- [81] Fan, L., Mao, Z. S., and Yang, C., 2004, "Experiment on Sedimentation of Slender Particles With Large Aspect Ratio and Correlation of Drag Coefficient," *J. Ind. Eng. Chem. Res.*, **43**(23), pp. 7664–7670.
- [82] Tran-Cong, S., Gay, M., and Michaelides, E. E., 2004, "Drag Coefficients of Irregularly Shaped Particles," *Powder Technol.*, **139**, pp. 21–32.
- [83] Hoerner, S. F., 1965, *Fluid-Dynamic Drag: Practical Information on Aerodynamic Drag and Hydrodynamic Resistance*, Hoerner Fluid Dynamics, Midland Park, NJ.
- [84] Mando, M., and Rosendahl, L., 2010, "On the Motion of Non-Spherical Particles at High Reynolds Number," *Powder Technol.*, **202**, pp. 1–13.
- [85] Mao, Z. S., 2008, "Knowledge on Particle Swarm: The Important Basis for Multi-scale Numerical Simulation of Multiphase Flows," *Chin. J. Process Eng.*, **8**(4), pp. 645–659. Available at http://en.cnki.com.cn/Article_en/CJFDTotal-HGYJ200804004.htm
- [86] Feng, Y., 2013, "Computational Analysis of Non-spherical Particle Dynamics in Airflow With Applications to Particle Transport and Deposition in Human Respiratory Models," Ph.D. thesis, NC State University, Raleigh, NC.
- [87] Goldstein, H., Poole, C. P., and Safko, J., 1980, *Classical Mechanics*, Addison-Wesley, Boston, MA.
- [88] Clift, R., Grace, J. R., and Weber, M. E., 2005, *Bubbles, Drops, and Particles*, Dover Publications, Inc., Mineola, New York.
- [89] Shenoy, A. R., and Kleinstreuer, C., 2008, "Flow Over a Thin Circular Disk at Low to Moderate Reynolds Numbers," *J. Fluid Mech.*, **605**, pp. 253–262.
- [90] Shanley, K. T., and Ahmadi, G., 2011, "A Numerical Model for Simulating the Motion of Ellipsoidal Fibers Suspended in Low Reynolds Number Shear Flows," *Aerosol Sci. Technol.*, **45**, pp. 838–848.
- [91] Brenner, H., 1963, "The Stokes Resistance of An Arbitrary Particle," *Chem. Eng. Sci.*, **18**, pp. 1–25.
- [92] Fan, F. G., and Ahmadi, G., 1995, "A Sublayer Model for Wall Deposition of Ellipsoidal Particles in Turbulent Streams," *J. Aerosol Sci.*, **26**(5), pp. 813–840.
- [93] Richter, A., and Nikrityuk, P. A., 2012, "Drag Forces and Heat Transfer Coefficients for Spherical, Cuboidal and Ellipsoidal Particles in Cross Flow at Sub-Critical Reynolds Numbers," *Int. J. Heat Mass Transfer*, **55**, pp. 1343–1354.
- [94] Harper, E. Y., and Chang, I., 1968, "Maximum Dissipation Resulting from Lift in a Slow Viscous Shear Flow," *J. Fluid Mech.*, **33**(Part 2), pp. 209–225.
- [95] Drew, D. A., and Lahey, R. T., Jr., 1987, "The Virtual Mass and Lift Force on a Sphere in Rotating and Straining Flow," *Int. J. Multiphase Flow*, **25**(6/7), pp. 1321–1372.
- [96] Auton, T. R., 1987, "The Lift Force on a Spherical Body in a Rotational Flow," *J. Fluid Mech.*, **183**, pp. 199–218.
- [97] Longest, P. W., and Xi, J., 2007, "Effectiveness of Direct Lagrangian Tracking Models for Simulating Nanoparticle Deposition in the Upper Airways," *Aerosol Sci. Technol.*, **41**, pp. 380–397.
- [98] Jeffery, G. B., 1922, "The Motion of Ellipsoidal Particles Immersed in a Viscous Fluid," *Proc. R. Soc. A*, **102**, pp. 161–179.
- [99] Chu, K. W., and Yu, A. B., 2008, "Numerical Simulation of Complex Particle-Fluid Flows," *Powder Technol.*, **179**(3), pp. 104–114.
- [100] Cundall, P. A., and Strack, O. D. L., 1979, "A Discrete Numerical Model for Granular Assemblies," *Geotechnique*, **29**, pp. 47–65.
- [101] O'Sullivan, C., 2011, *Particulate Discrete Element Modelling: A Geomechanics Perspective*, Spon Press, Florence, KY.
- [102] Kafui, K. D., Thornton, C., and Adams, M. J., 2002, "Discrete Particle-Continuum Fluid Modelling of Gas-Solid Fluidised Beds," *Chem. Eng. Sci.*, **57**, pp. 2395–2410.
- [103] Campbell, C. S., and Brennen, C. E., 1985, "Computer Simulation of Granular Shear Flows," *J. Fluid Mech.*, **151**, pp. 167–188.
- [104] Campbell, C. S., and Brennen, C. E., 1985, "Chute Flows of Granular Material: Some Computer Simulation," *ASME J. Appl. Mech.*, **52**(1), pp. 172–178.
- [105] Duran, J., 2000, *Sands, Powders, and Grains: An Introduction to the Physics of Granular Materials*, Springer, New York.
- [106] Zhu, H. P., Zhou, Z. Y., Yang, R. Y., Yu, A. B., 2007, "Discrete Particle Simulation of Particulate Systems: Theoretical Developments," *Chem. Eng. Sci.*, **62**, pp. 3378–3396.
- [107] Parry, A. J., and Millet, O., 2010, "Modeling Blockage of Particles in Conduit Constrictions: Dense Granular-Suspension Flow," *J. Fluid Eng.*, **132**, p. 011302.
- [108] Kloss, C., Goniva, C., Aichinger, G., and Pirker, S., 2009, "Comprehensive DEM-DPM-CFD Simulations-Model Synthesis, Experimental Validation and Scalability," Proceedings of the Seventh International Conference on CFD in the Minerals and Process Industries, CSIRO, Melbourne, Australia.
- [109] Tao, H., Jin, B., Zhong, W., Wang, X., Ren, B., Zhang, Y., and Xiao, R., 2010, "Discrete Element Method Modeling of Non-Spherical Granular Flow in Rectangular Hopper," *Chem. Eng. Process.*, **49**(2), pp. 151–158.
- [110] Zhou, Z. Y., Pinson, D., Zou, R. P., and Yu, A. B., 2009, "CFD-DEM Simulation of Gas Fluidization of Ellipsoidal Particles," Proceedings of the Seventh International Conference on CFD in the Minerals and Process Industries, CSIRO, Melbourne, Australia.
- [111] Zhou, Z. Y., Zou, R. P., Pinson, D., and Yu, A. B., 2011, "Dynamic Simulation of the Packing of Ellipsoidal Particles," *Indust. Eng. Chem. Res.*, **50**, pp. 9787–9798.
- [112] Ren, B., Zhong, W. Q., Jin, B. S., Yuan, Z. L., and Lu, Y., 2011, "Computational Fluid Dynamics (CFD)-Discrete Element Method (DEM)

- Simulation of Gas-Solid Turbulent Flow in a Cylindrical Spouted Bed With a Conical Base," [Energy Fuels](#), **29**(9), pp. 4095–4105.
- [113] Tian, L., 2008, "The Transport and Deposition of Ellipsoidal Fibers in Human Tracheobronchial Airways," Ph. D. thesis, Department of Mechanical and Aeronautical Engineering, Clarkson University, Potsdam, NY.
- [114] Gallily, I., and Eisner, A. D., 1979, "On the Orderly Nature of the Motion of Nonspherical Aerosol Particles: I. Deposition from a Laminar Flow," [J. Colloid Interface Sci.](#), **68**(2), pp. 320–337.
- [115] Chen, Y. K., and Yu, C. P., 1991, "Sedimentation of Fibers from Laminar Flows in a Horizontal Circular Duct," [Aerosol Sci. Technol.](#), **14**, pp. 343–347.
- [116] Högberg, S. M., Åkerstedt, H. O., Lundström, T. S., and Freund, J. B., 2010, "Respiratory Deposition of Fibers in the Non-inertial Regime—Development and Application of a Semi-analytical Model," [Aerosol Sci. Technol.](#), **44**(10), pp. 847–860.
- [117] Högberg, S. M., Åkerstedt, H. O., Holmstedt, E., Lundström, T. S., and Sandström, T., 2012, "Time-Dependent Deposition of Micro- and Nanofibers in Straight Model Airways," [J. Fluids Eng.](#), **134**, p. 051208.